

RingMo-Aerial: An Aerial Remote Sensing Foundation Model With Affine Transformation Contrastive Learning

Wenhui Diao[†], Haichen Yu[†], Kaiyue Kang[†], Tong Ling[†], Di Liu, Yingchao Feng, Hanbo Bi, Libo Ren, Xuexue Li, Yongqiang Mao, Xian Sun

Abstract—Aerial Remote Sensing (ARS) vision tasks pose significant challenges due to the unique characteristics of their viewing angles. Existing research has primarily focused on algorithms for specific tasks, which have limited applicability in a broad range of ARS vision applications. This paper proposes the RingMo-Aerial model, aiming to fill the gap in foundation model research in the field of ARS vision. By introducing the Frequency-Enhanced Multi-Head Self-Attention (FE-MSA) mechanism and an affine transformation-based contrastive learning pre-training method, the model's detection capability for small targets is enhanced and optimized for the tilted viewing angles characteristic of ARS. Furthermore, the ARS-Adapter, an efficient parameter fine-tuning method, is proposed to improve the model's adaptability and effectiveness in various ARS vision tasks. Experimental results demonstrate that RingMo-Aerial achieves SOTA performance on multiple downstream tasks. This indicates the practicality and efficacy of RingMo-Aerial in enhancing the performance of ARS vision tasks.

Index Terms—Aerial Remote Sensing (ARS), Foundation Model, Contrastive Learning(CL), Affine Transformation

1 INTRODUCTION

AERIAL Remote Sensing (ARS) is an essential method of data acquisition, distinct from aerospace remote sensing (ApRS) in its flexibility, as it is typically free from constraints such as revisit cycles, satellite sensor incidence angles, and timing limitations. ARS sensors, usually mounted on Unmanned Aerial Vehicles (UAVs), airplanes, or balloons, offer advantages over satellite-based remote sensing by quickly reaching target areas and capturing real-time, multi-perspective observations at various resolutions. This capability enables ARS to provide detailed information in applications ranging from emergency response to environmental monitoring and national defense. Thus, enhancing intelligent information extraction from ARS images holds significant academic and practical value.

- *W. Diao, H. Yu, K. Kang, and T. Ling labeled with † contribute equally to this work.*
- *This work was supported by the National Nature Science Foundation of China under Grant 62331027. (Corresponding authors: Xian Sun.)*
- *W. Diao, H. Yu, K. Kang, T. Ling, H. Bi, L. Ren, X. Li, and X. Sun are with the Aerospace Information Research Institute, Chinese Academy of Sciences, Beijing 100190, China, also with the School of Electronic, Electrical and Communication Engineering, University of Chinese Academy of Sciences, Beijing 100190, China, also with the University of Chinese Academy of Sciences, Beijing 100190, China, and also with the Key Laboratory of Target Cognition and Application Technology (TCAT), Aerospace Information Research Institute, Chinese Academy of Sciences, Beijing 100190, China (e-mail: diaowh@aircas.ac.cn, yuhaichen18@mails.ucas.ac.cn, kangkaiyue23@mails.ucas.ac.cn, lingtong23@mails.ucas.ac.cn, sunxian@aircas.ac.cn).*
- *Y. Mao is with the Department of Electronic Engineering, Tsinghua University, Beijing 100084, China.*
- *D. Liu and Y. Feng are with the Aerospace Information Research Institute, Chinese Academy of Sciences, Beijing 100190, China, and also with the Key Laboratory of Target Cognition and Application Technology (TCAT), Aerospace Information Research Institute, Chinese Academy of Sciences, Beijing 100190, China.*

Despite ARS's distinct advantages and applications, research efforts in intelligent remote sensing interpretation are still largely focused on ApRS imagery. As shown in Fig.1, although interest in ARS has grown rapidly in recent years, studies in its intelligent interpretation remain relatively limited, with publications in this area comprising less than 10% of ApRS-related work.

Unlike ApRS, ARS imagery is characterized by unique physical properties, including multi-view perspectives, varied resolutions, and occlusion effects, due to its flexible observational angles and sensor characteristics, as shown in Fig.2. In Fig.2(a), various perspectives are depicted, including oblique views (i and ii), a vertical view (iii), and a horizontal view (iv). Unlike ApRS, which predominantly captures vertical views, ARS imagery often incorporates oblique angles, providing more dimensional perspectives of targets. However, this also results in distant objects appearing smaller and more densely arranged, increasing the complexity of image interpretation. Fig.2(b) shows images at low, medium, and high resolutions (i, ii, iii, respectively), reflecting the diverse resolutions produced by ARS sensors at varying altitudes and speeds. Such differences in resolution affect target clarity and detail across images, placing higher demands on model adaptability. Additionally, significant occlusion is common in aerial imagery, as demonstrated in Fig.2(c), where some targets are partially or fully obscured by other objects, further complicating image interpretation.

These challenges highlight the need for specialized intelligent models tailored to ARS applications. While recent foundational models in computer vision and RS have shown potential, they are often inadequate for ARS due to its unique requirements. These models benefit from pre-training on vast amounts of data and large-scale parameters,

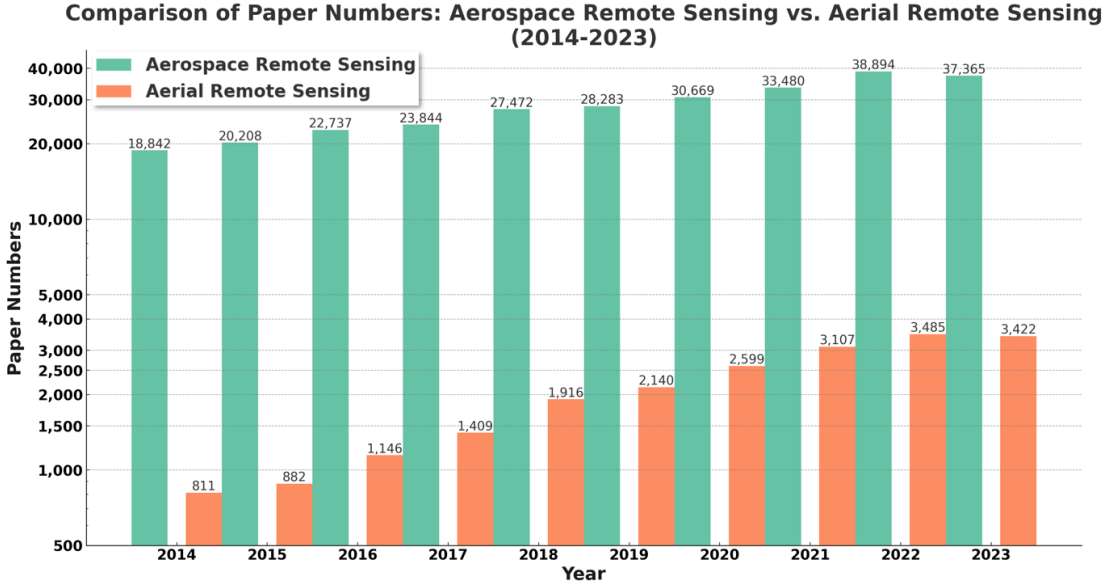


Fig. 1. Number of Aerospace Remote Sensing and Aerial Remote Sensing papers in Web of Science in the last decade. The green bars represent aerospace remote sensing, while the orange bars represent aerial remote sensing. Although research on ARS has grown, the number of papers remains significantly lower than that of aerospace remote sensing.

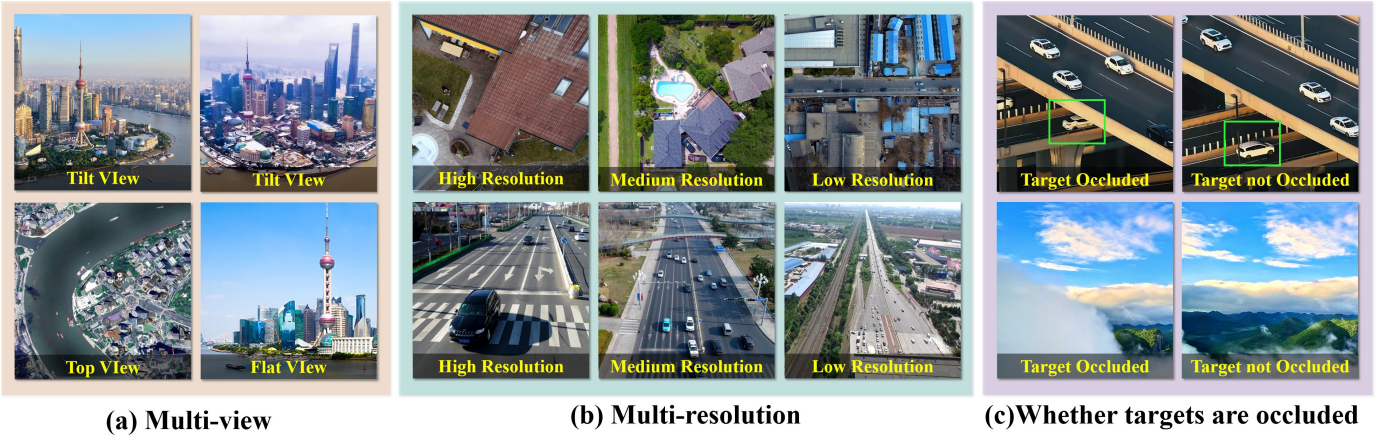


Fig. 2. Illustration of multi-view, multi-resolution, and occlusion of ARS images: (a) Multi-view imagery shows images captured from different angles, including tilt, top, and flat views; (b) Multi-resolution imagery demonstrates how varying low, medium, and high resolutions affect the level of detail; (c) Target occlusion compares cases where the target is partially occluded versus not occluded. These characteristics highlight the complexity of ARS imagery in different scenarios.

enabling them to adapt more rapidly and effectively to various changes.

However, current foundational model research primarily focuses on ApRS imagery, as evidenced by studies like RingMo [1] and Skysense [2]. This underscores the need for a dedicated pre-trained foundational model specifically designed for ARS. Adapting existing foundational models for ARS involves addressing several critical challenges:

(1) Challenges in Pre-training: Pre-training generally relies on large-scale datasets for self-supervised learning, primarily using Masked Image Modeling (MIM) and Contrastive Learning (CL). MIM, employed by models like MAE [3] and SimMIM [4], masks parts of images for reconstruction to enhance feature extraction, while CL, seen in models like MOCO [5], leverages positive and negative sample pairs to learn relational features. Both methods have merits but

also limitations; MIM is widely used across visual tasks, as RingMo [1]. However, ARS images vary significantly in features due to differences in perspective and resolution. As shown in Fig.3, the vertical view displays structured, continuous features with broad areas of color consistency, containing abundant low-frequency information. In contrast, the oblique view, capturing building sides and heights, offers dynamic perspectives with high detail variability and lower low-frequency content. Current methods, which often focus on reconstructing local image information, struggle to capture these unique variations in ARS imagery.

(2) Challenges in Fine-tuning: The traditional approach of global fine-tuning of models faces significant challenges, mainly due to the fact that fine-tuning may lead to overfitting, especially in ARS. Unlike single viewpoints and resolutions that are common in spatial remote sensing, ARS

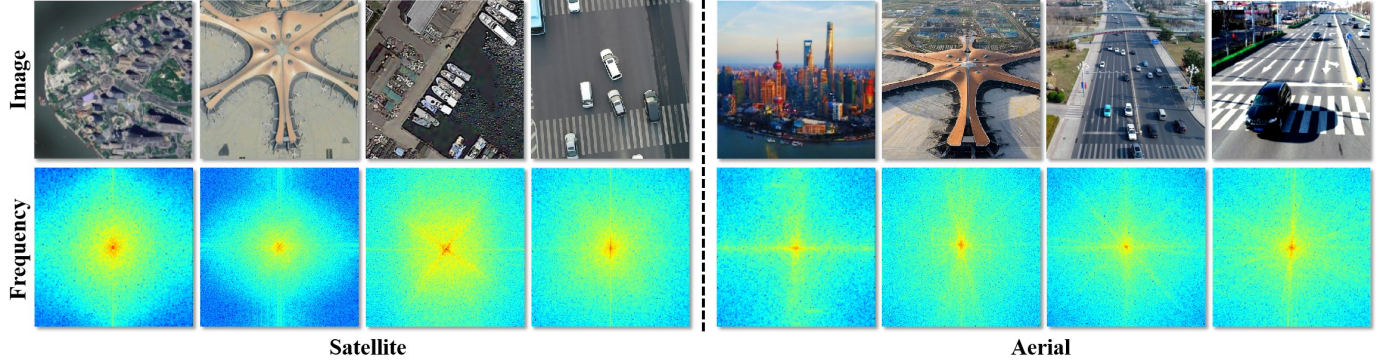


Fig. 3. Schematic Comparison of ApRS and ARS Image Features. Satellite images contain more low-frequency information with continuous features, while aerial images have more detailed variations and relatively less low-frequency information.

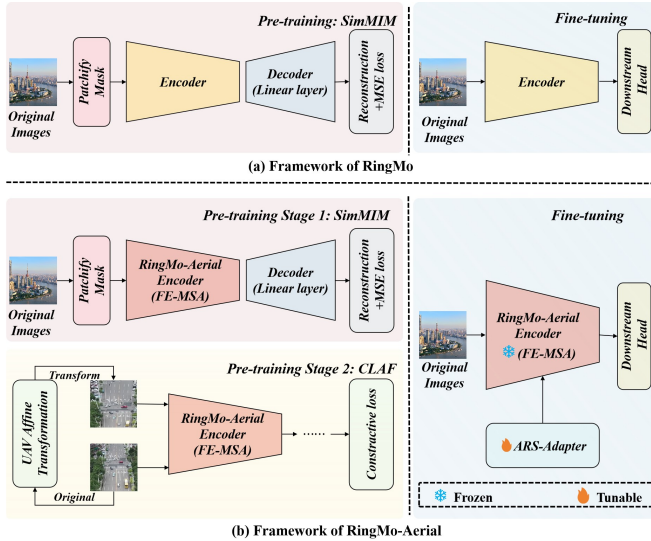


Fig. 4. Comparison of model frameworks between RingMo and RingMo-Aerial. (a) RingMo uses SimMIM for pre-training to perform image reconstruction. (b) RingMo-Aerial builds upon this by introducing affine transformation and contrastive learning, enhancing its ability to process multi-view images. In the fine-tuning stage, the ARS adapter is introduced to adjust a small number of parameters, further enhancing the model's generalization ability for downstream tasks.

models are more likely to be overfitted with specific viewpoints and resolutions for specific downstream tasks. This overfitting reduces the ability of the model to generalize to different viewpoints and resolutions in various downstream tasks.

To address the challenges above, we introduce RingMo-Aerial, the first foundational large model explicitly designed for ARS tasks. Building on the existing ApRS foundational model RingMo, RingMo-Aerial addresses the unique characteristics of ARS tasks through several novel approaches, as illustrated in Fig. 4.

First, we propose the Frequency-Enhanced Multi-Head Self-Attention (FE-MSA) module, designed to address the multi-scale and occlusion challenges inherent to oblique perspectives in ARS imagery. Unlike traditional multi-head attention mechanisms, FE-MSA includes an image patch expansion layer to capture dense, small objects as tokens for the Transformer model, leveraging Swin Transformer's

window and shifted window attention. This enhances the model's ability to detect densely packed and occluded objects.

Second, to improve detection and recognition of distant small targets in oblique views, we propose the Contrastive Learning Affine Framework (CLAF). CLAF uses affine transformations to scale and enlarge distant targets, constructing positive samples to guide the model in learning ARS-specific visual features.

In addition, during the fine-tuning phase, we propose an efficient fine-tuning method for basic ARS foundational models called ARS-Adapter. Unlike traditional comprehensive fine-tuning methods, ARS-Adapter achieves efficient model fine-tuning by adjusting fewer than 5% of the parameters, significantly improving the training efficiency of downstream tasks while reducing the risk of overfitting. ARS-Adapter applies to all layers of the model: in the attention layers, it employs a traditional Adapter [6] structure that operates parallel to the attention layers; in the Multi-Layer Perceptron (MLP) layers, it utilizes a bottleneck structure that includes MLP downsampling, deep convolutional feature extraction, and MLP upsampling. This approach optimizes the performance of the ARS foundational model, making it more adaptable and effective across various ARS vision tasks.

In summary, the contributions of this paper can be summarised as follows:

- **Addressing ARS-specific Characteristics:** We introduce RingMo-Aerial, the first foundational model for ARS, supporting multi-perspective, multi-resolution, and multi-modality tasks across various applications.
- **FE-MSA Module:** By incorporating a patch expansion layer and integrating the window attention mechanism, FE-MSA effectively enhances the detection capability of small, dense targets in ARS images.
- **CLAF Module:** CLAF uses affine transformations to capture ARS-specific visual features, particularly in oblique perspectives, improving the model's recognition of distant objects.
- **ARS-Adapter:** The ARS-Adapter provides a fine-tuning approach tailored to ARS models, enhancing efficiency and reducing overfitting risks.

To evaluate the effectiveness of the model, we performed six downstream tasks using 13 ARS datasets and 5 ApRS

datasets with different viewpoints, resolutions, and modes. The test results show that RingMo-Aerial achieves SOTA performance on all ARS datasets and reaches the leading level on ApRS datasets, which proves its strong generalization ability for intelligent interpretation of aerial and ApRS images. Compared with the single-task model, RingMo-Aerial has apparent advantages in handling multi-tasks in different scenarios.

2 RELATED WORK

2.1 Aerial remote sensing(ARS)

ARS offers unique characteristics and applications across various domains, supporting tasks such as object detection, object tracking, semantic segmentation, and 3D reconstruction. The most frequently utilized modalities are optical imaging [7], infrared imaging [8], and synthetic aperture radar (SAR) [9].

Compared to ApRS, ARS enables higher image resolution and flexible spatiotemporal coverage. However, it also presents distinct characteristics. Aerial imagery is typically captured at oblique angles with varying distances, leading to differences in target sizes and an increased likelihood of occlusion. For example, [10], [11], [12], [13] addressed target occlusion by modeling occluded objects at the structural level, significantly enhancing detection and segmentation performance. Studies such as [14], [15], [16], [17] have improved small target resolution by optimizing for oblique perspectives through multi-scale transformations.

Another critical difference lies in the frequency content of ARS imagery. Unlike ApRS images, which primarily capture low-frequency information, aerial images contain a mix of high-frequency and low-frequency signals, enabling detailed image interpretation. Recent work [18], [19] introduced frequency-domain enhancement modules to balance these signals, thereby improving performance across various ARS tasks.

2.2 Visual foundation model

Visual foundation models have gained attention as general-purpose solutions for computer vision tasks. Early models, based on convolutional neural networks (CNNs) like VGG [20] and ResNet [21], used convolutional layers for feature extraction and were typically pre-trained on classification tasks using ImageNet [22]. With the advent of Transformers in natural language processing, visual Transformer models like ViT [23], and Swin Transformer [24] have gained prominence, utilizing masked image modeling (MIM) or contrastive learning (CL) for self-supervised pre-training. In the field of remote sensing (RS), models such as RingMo [1] and SkySense [2] have adopted the visual Transformer architecture and self-supervised pre-training strategies. Several novel architectures, such as ConvNeXt [25] and Mamba [26], have been proposed. However, these newer models have yet to achieve widespread adoption due to technical immaturity.

A major challenge for these models lies in the pre-training phase, where they learn broad visual representations from large datasets. This section provides an overview of three self-supervised training methods—contrastive

learning, masked image modeling, and their combination—each addressing both natural and RS images.

2.2.1 Contrastive Learning

Contrastive learning is a self-supervised learning approach that emphasizes learning the standard features among similar instances while distinguishing differences between dissimilar cases. Primary contrastive learning methods include the MoCo [5], [27], [28] series. MoCov2 [27], an optimization of MoCo [5] inspired by SimCLR [29], introduces enhancements such as the MLP projection head and increased data augmentation. MoCov3 [28] integrates MoCov2 and SimSiam [30], but training with ViT [23] as the backbone often leads to instability and reduced model accuracy. Stability and performance are improved by freezing the patch projection layer of ViT during training. DINO [31], another self-supervised learning method, employs knowledge distillation techniques to train ViT for semantic segmentation and classification feature learning without labels, leveraging momentum encoders and multi-crop training for enhanced model performance.

In RS, contrastive learning also has many applications. GLCNet [32] presents a self-supervised contrastive learning method for semantic segmentation of high-resolution RS images. SeCo [33] introduces a self-supervised pre-training method that leverages temporal information in RS images to generate positive sample pairs, learning feature representations invariant and diverse to seasonal variations.

2.2.2 Masked Image Modeling

MIM is an emerging self-supervised pre-training method. It involves masking a portion of an input image and then reconstructing it through a pretext task. Unlike traditional supervised pre-training, which relies on labeled data, MIM uses self-supervised learning to learn meaningful representations from images. MAE [3] pioneered the MIM by masking and reconstructing images using Vision Transformer (ViT). SimMIM [4] differs by only reconstructing masked areas and incorporates the Swin Transformer [24]. Combining MAE and SimMIM, MixMAE [34] uses visible tokens from different images for reconstruction. GreenMIM [35] optimizes MAE by introducing a layered architecture to lower computational costs. UM-MAE [36] applies uniform masking to address complexities in ViTs, while CAE [37] adds a regressor for distinct feature encoding separate from reconstruction.

In RS, RingMo [1] pioneered the foundation model framework based on MIM. Unlike random masking techniques used in natural scenes, RingMo developed the PI-Mask strategy tailored to the complex backgrounds and small targets characteristic of RS data, focusing on preserving information about small targets. By integrating ViT and Swin Transformer, RingMo enhanced the accuracy of various downstream RS tasks, laying a foundation for developing large models in RS scenes.

2.2.3 The combination of Contrastive Learning & Masked Image Modeling

Combining CL and MIM has shown significant advantages in current research, particularly in enhancing feature extrac-

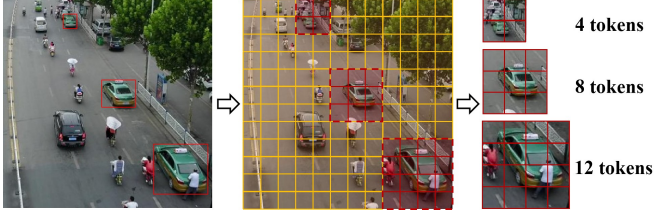


Fig. 5. Similar targets with significant size differences in the same picture. In the Vision Transformer model, objects of different sizes occupy different numbers of tokens. The image is from the VisDrone dataset.

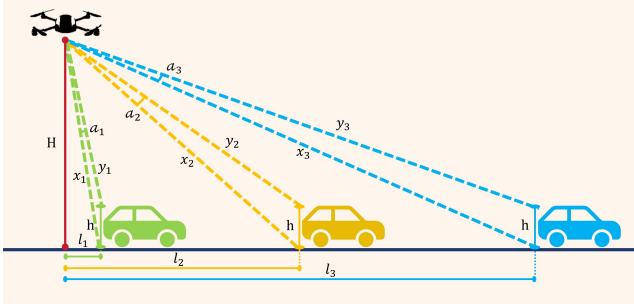


Fig. 6. The same target will be represented differently in the image if its distance from the lens and imaging angle are different. As the horizontal distance increases, the number of pixels occupied by the height content increases and then decreases, and the height content occupies the most pixels at the horizontal distance $l = \sqrt{H(H-h)}$.

tion performance. For instance, CMAE [38] utilizes an asymmetric encoder-decoder structure along with a momentum encoder. This enables learning visual representations from masked images and enhances feature discriminability through CL. Additionally, MimCo [39] introduces patch-level and image-level contrastive reconstruction losses in MIM, effectively improving the model's transferability.

In the field of RS, TMAC [40] and SegMind [41] demonstrate that combining MIM and CL significantly improves the utilization of unlabeled data. It also enhances the interaction between different image regions, boosting feature recognition capabilities.

Despite the success of models like ViT and RingMo in general and satellite remote sensing tasks, their performance in ARS remains limited. Currently, there is no dedicated foundation model for ARS. To address this gap, we propose RingMo-Aerial, a model designed specifically for ARS tasks, and demonstrate its effectiveness in typical applications.

3 PROBLEM DESCRIPTION

The unique imaging properties of ARS photography stem from the inherent properties of aerial perspective. Specifically, this perspective manifests itself in size differences within the same image due to the tilted angle of the shot. As shown in Fig.5, similar objects at different distances from the ARS are rendered at different sizes in the image.

As shown in Fig.6, when the camera is positioned at a height H and the target object has a height h , the angular size α of the target's height in the camera's field of view varies as a function of the horizontal distance l between the target and the camera. At different horizontal distances, the imaging size corresponding to the same target height

differs. Specifically, when the target is directly beneath the camera, its height is not captured in the image. As the horizontal distance increases, the number of pixels occupied by the target's height initially increases and then decreases. By considering the distances from the target's lowest and highest points to the camera, given by $x = \sqrt{H^2 + l^2}$ and $y = \sqrt{(H-h)^2 + l^2}$ respectively, we can derive the relationship between the viewing angle α and the horizontal distance l between the target and the camera:

Using the cosine rule:

$$x^2 + y^2 - 2xy \cos \alpha = h^2 \quad (1)$$

Substituting the values of x and y , The final cosine formula becomes:

$$\cos \alpha = \frac{H^2 - Hh + l^2}{\sqrt{H^2 + l^2} \cdot \sqrt{(H-h)^2 + l^2}} \quad (2)$$

By setting $a = H$ and $b = H - h$, we have the target function is:

$$f(l) = \cos \alpha = \frac{ab + l^2}{\sqrt{a^2 + l^2} \cdot \sqrt{b^2 + l^2}} \quad (3)$$

Taking the derivative of $f(l)$:

$$f'(l) = \frac{2l(a^2 + l^2)(b^2 + l^2) - l(ab + l^2)(a^2 + b^2 + 2l^2)}{(a^2 + l^2)^{3/2}(b^2 + l^2)^{3/2}} \quad (4)$$

Solving $f'(l) = 0$ results in the equation:

$$2(a^2 + l^2)(b^2 + l^2) = (ab + l^2)(a^2 + b^2 + 2l^2) \quad (5)$$

Simplifying further:

$$2a^2b^2 + a^2l^2 + b^2l^2 = a^3b + ab^3 + 2abl^2 \quad (6)$$

Combining terms:

$$l^2(a - b)^2 = ab(a - b)^2 \quad (7)$$

Since $a = H$ and $b = H - h$, and $a > b$, it follows that $a - b = h > 0$.

When $f'(l) = 0$, we obtain:

$$l^2 = ab \quad (8)$$

Therefore:

$$l = \sqrt{ab} = \sqrt{H(H-h)} \quad (9)$$

This completes the derivation of the maximum value α and the corresponding minimum value $\cos \alpha$. From Eq. (2), when $l = 0$, α is equal to 0. From Eqs.(4) and (9), α increases with l is less than $\sqrt{H(H-h)}$, α is maximum when $l = \sqrt{H(H-h)}$, and decreases with l when l is greater than $\sqrt{H(H-h)}$, and decreases with l in the case of $l \rightarrow \infty$ when α is again equal to 0. Assuming that the optical axis of the camera is always at the center of the target viewpoint α , the pixel change of the target height information in the picture is the same as the change of the corresponding viewpoint α of the target. This indicates that if the same target is at different distances from the lens and imaging angles, it will have different representations in the image.

In the visual transformer model, the number of pixels occupied by an object is related to the number of tokens it occupies, as Fig.5. Therefore, it is helpful to adopt a method

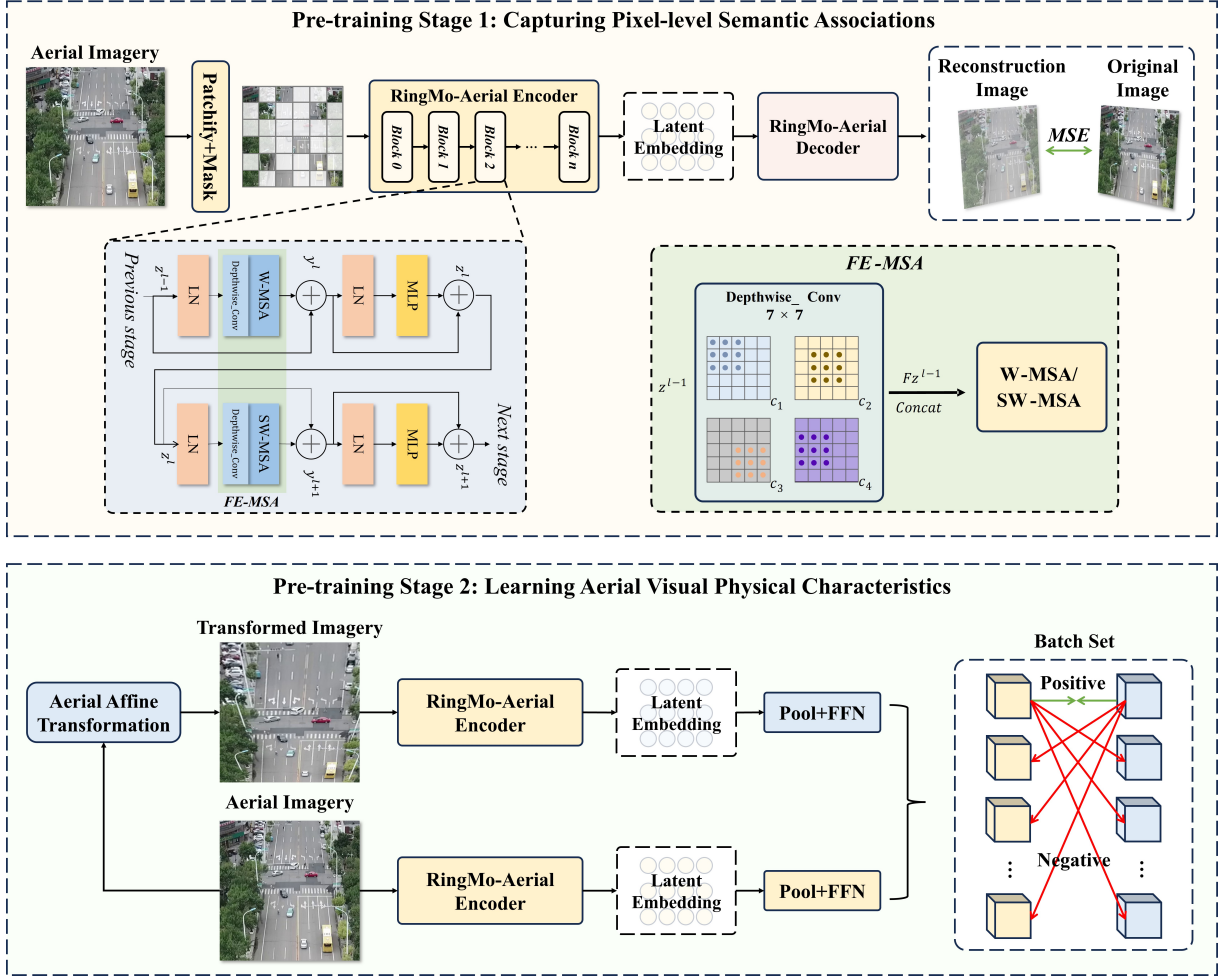


Fig. 7. RingMo-Aerial's two-stage pre-training principles Capturing Pixel-level Semantic Associations and Learning Aerial Visual Physical Characteristics, and the architecture of the FE-MSA module.

to balance the number of tokens occupied by similar objects of different sizes in an image.

In addition to the oblique angles, ARS images typically contain many small objects, which can be very dense. CNNs have fixed convolution kernel sizes and limited receptive fields, which makes it challenging to capture large-scale information and detailed information in ARS images simultaneously. This can result in missed detections and false detections of objects. For instance, when Sensors capture congested urban streets, pedestrians and vehicles may randomly occlude other objects, making it challenging for detection algorithms to locate and classify them accurately. ViT employs the same downsampling rate and directly extracts features from image tokens, which fails to account for the spatial context of objects.

Furthermore, ARS images are typically high resolution, containing many intricate details and complex background information. This places greater demands on pre-trained models' feature extraction and processing capabilities. Traditional pre-trained models are typically trained on large-scale natural scene datasets, which cannot adequately represent the characteristics of ARS images.

Consequently, a practical pre-training framework and method, specifically designed to address the distinctive

visual characteristics of ARS images, is essential to achieve satisfactory performance in a range of downstream tasks.

4 METHODOLOGY

4.1 Method Overview

The proposed RingMo-Aerial model serves as a foundational framework with broad applicability. Its implementation involves three main stages: model design, pre-training, and fine-tuning for downstream tasks. In Section 4.2, we address the challenge of detecting small objects in ARS imagery caused by oblique viewing angles during the model design phase. To enhance small object detection, we introduce the Frequency-Enhanced Multi-Head Self-Attention (FE-MSA) layer by incorporating a patch expansion layer, shown in Fig.7. In Section 4.3, we combine the commonly used masked image modeling (MIM) pre-training with additional contrastive learning (CL) methods based on affine transformations during the pre-training stage. This hybrid pre-training approach significantly improves both training speed and the performance of the converged model on downstream tasks, shown in Fig.7. Furthermore, in Section 4.4, we introduce a parallel Adapter fine-tuning method during the fine-tuning phase. The proposed ARS-Adapter module includes downsampling, channel-wise convolution,

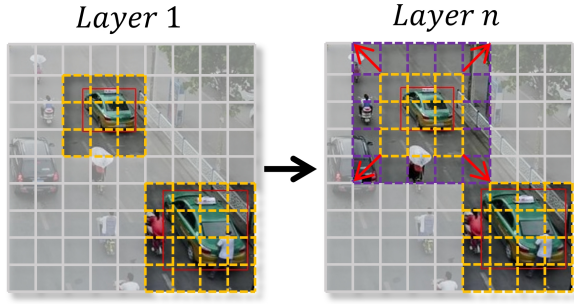


Fig. 8. The effect of FE-MSA. Existing window attention mechanisms cannot balance the feature vector information of objects of different sizes in the image. At the same time, FE-MSA enhances the model's receptive field for small objects (purple box).

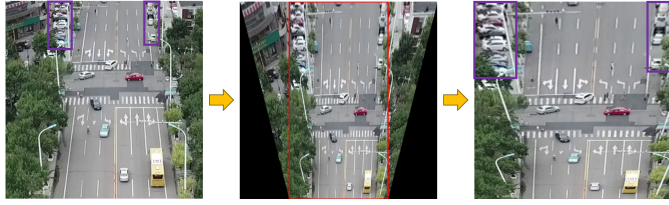


Fig. 9. Positive samples for contrastive learning are obtained after the image's affine transformation, cropping, and resizing.

and upsampling components, enhancing its adaptability and learning capacity for specific tasks.

4.2 Model Architecture

RingMo-Aerial's design is based on the RingMo. The architecture of the Swin Transformer consists of four stages, each comprising either a linear encoder or Patch Merging, along with an even number of Swin Transformer Blocks. Each block includes Window Multi-Head Self-Attention (W-MSA) and Shifted Window Multi-Head Self-Attention (SW-MSA). These attention mechanisms effectively compute attention maps within the windows, extracting spatial feature information between pixels while reducing the computational complexity of the model.

Although the classical Swin Transformer introduces spatial interactions through two types of window attention mechanisms, emphasizing high-level semantic information within feature vectors, challenges arise in ARS imagery. The varying shooting distances, angles, and scale differences between distant and nearby objects present significant difficulties. Relying solely on semantic information may not be sufficient to achieve optimal performance in downstream tasks.

To address the challenges above, we propose the overall architecture of RingMo-Aerial. As shown in Fig.7 Pre-training Stage 1, considering the unique characteristics of the ARS perspective and based on the window attention mechanisms (W-MSA and SW-MSA), a new attention mechanism called Frequency-Enhanced Multi-Head Self-Attention (FE-MSA) is introduced to enhance the model's capability in handling diverse aerial scenarios.

Frequency-Enhanced Multi-Head Self-Attention (FE-MSA) module. To better understand the FE-MSA mechanism, it is essential first to recognize the limitations of the

existing window attention mechanisms. These mechanisms often struggle to balance the semantic information in feature vectors of objects of different sizes. For instance, as illustrated in Fig.8, larger objects may occupy 4×4 tokens, while smaller distant objects may occupy only 3×3 tokens. The FE-MSA mechanism introduces frequency domain processing to the existing window attention, indirectly expanding the receptive field for smaller objects.

Fig.7(b) illustrates the RingMo-Aerial Block structure, including two window attention mechanisms optimized by the FE-MSA mechanism. Given $z^{(l-1)} \in \mathbb{R}^{\frac{W}{4} \times \frac{H}{4} \times C}$, where l is the id of each RingMo-Aerial Block. Taking the first stage as an example, the input feature vector z^l adopts the same slicing parameters as the standard Swin-Transformer, resulting in four-channel slices $C = \{c_1, c_2, c_3, c_4\}$. After linear normalization, it enters the FE-MSA module. For each patch with a dimension of C , a 7×7 convolution kernel is used for depthwise convolution to obtain the feature map $Fz^{(l-1)} = \text{Concat}\{Fc_1, Fc_2, Fc_3, Fc_4\}$. Then, W-MSA or SW-MSA is used to compute the attention map. After the FE-MSA, small objects' edge and texture features are further enhanced, improving the model's ability to perceive local and global features. The computation process for each token patch through the RingMo-Aerial block is as follows:

$$z^l = \text{FE-MSA}(z^{l-1}) \quad (10)$$

$$\text{FE-MSA}(z^{l-1}) = \text{SoftMax}\left(\frac{qk^T}{\sqrt{d}} + B\right)v \quad (11)$$

The FE-MSA mechanism enables RingMo-Aerial to effectively capture edge and texture features of different targets in ARS images, improving the model's performance in complex aerial scenes. Fig.10 presents a comparative analysis of the feature extraction capabilities of the RingMo-Aerial and RingMo models in processing multiview ARS images. The heatmaps generated by RingMo-Aerial show more focused attention on critical areas, such as vehicles and buildings, as indicated by the bright regions. In contrast, the RingMo in the lower half has a more diffuse focus, with less concentration on specific features. This comparison demonstrates the superior ability of RingMo-Aerial to handle complex aerial scenes, enabling better feature extraction and object recognition in multiview ARS images. These results visually confirm the improvements introduced by RingMo-Aerial, particularly in addressing challenges such as varying scales and perspectives in aerial imagery.

4.3 Pre-training

For pre-training, we construct a large-scale pre-training dataset. Our comprehensive pre-training dataset covers a wide range of aerial scenes, including high-altitude, low-altitude, and near-ground perspectives. It spans diverse geographical regions such as urban, rural, and wilderness areas. The dataset includes various targets, such as roads, vehicles, and pedestrians, and captures different seasons and periods. Notably, it exhibits multi-source, multi-temporal, and multi-instance characteristics. Before training, we crop the entire dataset into 640×640 or 448×448 resolution slices, all captured using optical three-channel imaging. The sliced dataset comprises approximately 5.4 million images (Fig.11).

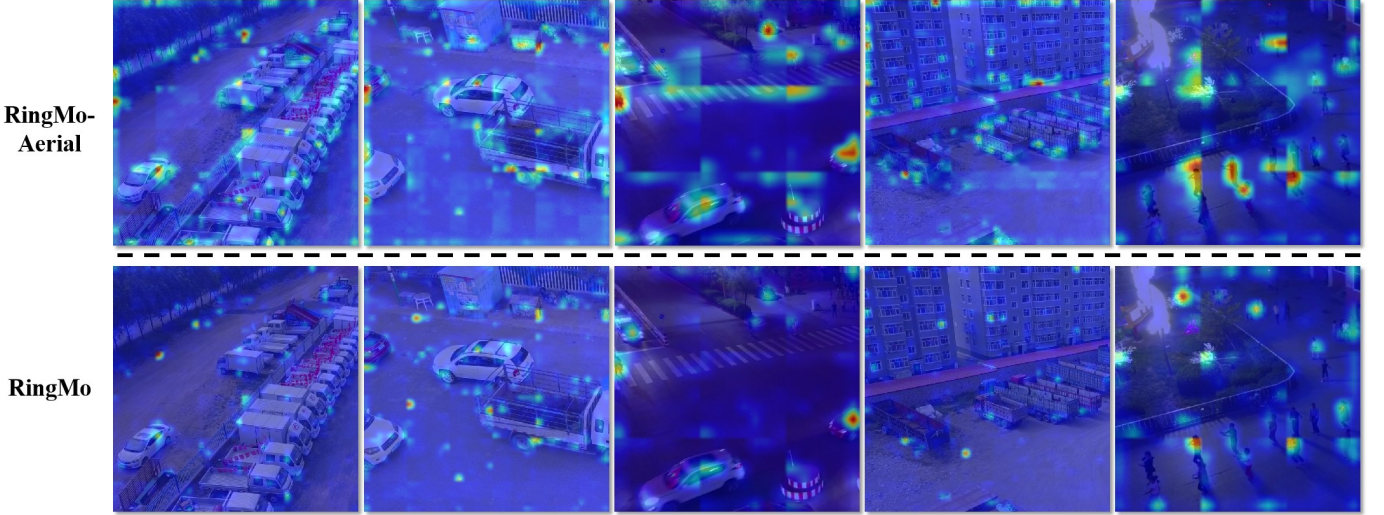


Fig. 10. Comparative analysis of feature heatmaps extracted from multi-view aerial imagery using RingMo-Aerial and RingMo. The feature heatmaps extracted by the RingMo-Aerial model are located in the upper half, while those from the RingMo model are in the lower half of the figure. In these images, the brighter the region, the more the model is focusing on that particular feature, indicating that these areas have higher feature importance for the model.

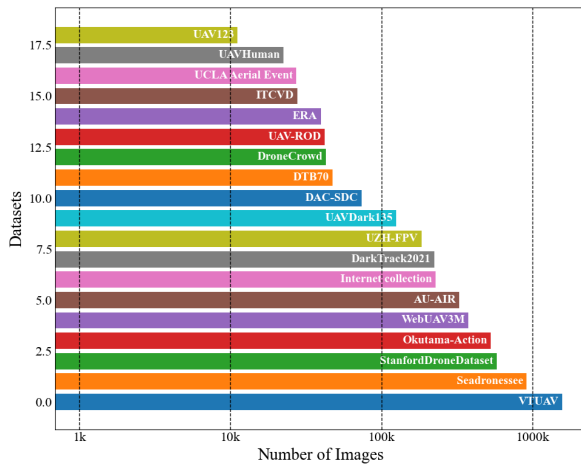


Fig. 11. The figure shows the number of slices corresponding to the slicing process performed on multiple collected open source airborne remote sensing datasets, which were used as the dataset for pre-training of the base model.

During the pre-training phase, we combine Masked Image Modeling (MIM) and Contrastive Learning (CL) techniques. For MIM training, we use the standard SimMIM pre-training framework. The primary goal of this approach is to enhance the model's ability to capture pixel-level semantic associations, thus initially equipping the model with feature extraction capabilities. However, as analyzed previously, solely using the MIM pre-training method for ARS foundational model training is insufficient for the model to learn the intrinsic object characteristics specific to ARS vision. Therefore, building upon the MIM pre-training, we propose a contrastive learning framework based on affine transformations. This involves generating positive and negative image pairs through affine transformations, which serve as the basis for the contrastive learning pre-training of the model.

The process of affine transformation of an image is completed through perspective transformation. Perspective transformation first defines the source point and the destination point, which are defined as:

$$\text{src_points} = \begin{bmatrix} x_0 & y_0 \\ x_1 & y_1 \\ x_2 & y_2 \\ x_3 & y_3 \end{bmatrix}, \quad \text{dst_points} = \begin{bmatrix} u_0 & v_0 \\ u_1 & v_1 \\ u_2 & v_2 \\ u_3 & v_3 \end{bmatrix} \quad (12)$$

The transformation relationship between the source point and the destination point used in the proposed method is:

$$\text{dst_points} = \begin{bmatrix} u_0 & v_0 \\ u_1 & v_1 \\ u_2 & v_2 \\ u_3 & v_3 \end{bmatrix} = \begin{bmatrix} x_0 & y_0 \\ x_1 & y_1 \\ \alpha x_2 + (1 - \alpha)x_3 & y_2 \\ \alpha x_3 + (1 - \alpha)x_2 & y_3 \end{bmatrix} \quad (13)$$

Among them, α is the transformation coefficient, and the value range is randomly between 0.05 and 0.35. On this basis, the perspective transformation matrix can be calculated. The perspective transformation matrix is defined as a 3×3 matrix in the form of:

$$M = \begin{bmatrix} m_{11} & m_{12} & m_{13} \\ m_{21} & m_{22} & m_{23} \\ m_{31} & m_{32} & 1 \end{bmatrix} \quad (14)$$

The solution process of this transformation matrix is as follows:

$$\begin{cases} u_i = \frac{m_{11}x_i + m_{12}y_i + m_{13}}{m_{31}x_i + m_{32}y_i + 1} \\ v_i = \frac{m_{21}x_i + m_{22}y_i + m_{23}}{m_{31}x_i + m_{32}y_i + 1} \end{cases} \quad \text{for } i = 0, 1, 2, 3 \quad (15)$$

Based on formulas (12) and (13), the above transformation matrix can be solved by the least square method. After obtaining the transformation matrix, the point (x, y) on the source image can be mapped to the point (u, v) on the destination image:

TABLE 1
Semantic Segmentation: Comp. on UAVID

Methods	Building		Tree		Clutter		Road		Low vegetation		Static car		Moving car		Human		mAcc	mIoU
	Acc	IoU	Acc	IoU	Acc	IoU	Acc	IoU	Acc	IoU	Acc	IoU	Acc	IoU	Acc	IoU		
DeeplabV3+ [42]	82.5	80.6	78.1	73.9	71.8	45.3	77.9	65.2	58.3	45.3	45.8	24.2	70.2	53.3	8.2	1.8	61.6	48.7
DANet [43]	81.8	81.2	80.2	72.3	69.3	46.1	78.2	63.6	56.9	46.2	48.3	23.8	70.8	54.2	8.6	3.0	61.8	48.8
ACNet [44]	82.3	81.6	80.8	72.6	68.9	45.3	79.4	64.1	57.3	46.5	48.1	23.2	71.2	55.0	8.8	3.2	62.1	48.9
OCRNet [45]	81.9	81.4	80.6	72.4	69.2	46.0	78.6	63.7	57.0	46.4	48.5	23.7	71.0	54.8	8.5	2.9	61.9	48.9
SETR [46]	82.3	78.9	78.3	71.2	66.9	45.8	76.2	63.8	60.6	43.7	45.6	22.6	70.1	54.8	7.8	1.6	61.0	47.8
Segformer [47]	83.6	81.2	80.3	74.1	70.3	46.3	76.8	64.6	61.0	46.2	45.3	24.6	70.3	56.1	12.2	5.3	62.5	49.8
C-Swin [48]	86.3	82.8	80.6	75.6	68.9	49.2	79.2	66.3	61.2	47.8	48.3	26.9	70.6	55.0	16.5	10.8	64.0	51.8
UAVFormer [49]	88.5	81.5	82.3	76.2	67.5	48.8	78.6	67.1	63.8	48.5	49.6	28.8	71.2	62.2	19.3	12.5	65.1	53.2
BiSeNetV2 [50]	-	81.6	-	76.0	-	61.2	-	77.1	-	61.3	-	38.5	-	66.4	-	15.4	-	59.7
Segmenter [51]	-	84.4	-	76.1	-	64.2	-	79.8	-	57.6	-	34.5	-	59.2	-	14.2	-	58.7
CoaT [52]	-	88.5	-	79.3	-	69.0	-	80.0	-	62.0	-	59.1	-	70.0	-	18.9	-	65.8
BANet [53]	-	85.4	-	78.9	-	66.6	-	80.7	-	62.1	-	52.8	-	69.3	-	21.0	-	64.6
UNetFormer [54]	-	87.4	-	80.2	-	68.4	-	81.5	-	63.5	-	56.4	-	73.6	-	31.0	-	67.8
RingMo(U) [1]	90.9	85.4	82.6	74.3	73.1	56.8	81.6	73.7	71.9	58.2	69.9	58.3	75.4	67.5	27.4	21.0	71.6	61.9
RingMo-Aerial(U)*	92.6	83.8	88.5	77.2	78.4	65.5	87.5	80.2	73.3	60.7	72.5	65.3	84.4	71.6	34.8	26.9	76.5	66.4
RingMo-Aerial(A)*	92.4	83.5	89.0	77.7	77.2	63.5	85.8	79.4	75.2	60.4	60.5	53.4	85.7	72.7	28.5	24.7	74.3	64.4
RingMo-Aerial(M)*	93.2	85.7	89.8	79.0	79.0	66.3	87.8	82.0	76.8	62.0	72.5	65.5	88.9	76.6	41.3	32.7	78.7	68.7

* Swin-Base (U) uses the Swin-Base backbone plus the UperNet segmentation algorithm. RingMo-Aerial (U), (A), (M) represent the RingMo aerial backbone with UperNet segmentation algorithm, ARS-Adapter and UperNet algorithm, and Mask2Former algorithm. Same below.

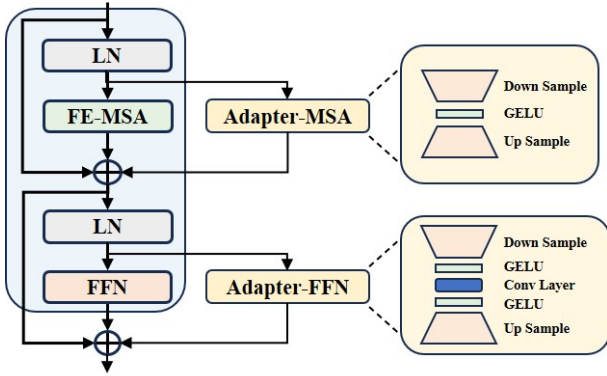


Fig. 12. ARS-Adapter is an enhancement module designed to improve transformer models by adding efficient, low-cost adaptation layers. It integrates down-sampling, activation (e.g., GELU), and up-sampling, optionally including convolution, to enrich feature representations while reducing computational overhead.

$$\begin{bmatrix} u \\ v \\ 1 \end{bmatrix} = M \cdot \begin{bmatrix} x \\ y \\ 1 \end{bmatrix} \quad (16)$$

We obtain the source image I_i and the transformed image I'_i through the aforementioned affine transformation process. The source image I_i and its corresponding transformed image I'_i form a positive sample pair, while the remaining sample pairs I_i and I'_j (where $i \neq j$) form negative sample pairs. By calculating the contrastive loss, we guide the model in learning the invariant properties of the transformation process, thereby training the model's ability to extract visual physical characteristics.

4.4 Downstream Fine-tuning

In the methodological section of the paper, we expand upon the fine-tuning strategies employed for downstream tasks. Beyond the conventional approach of fine-tuning the entire model, this study introduces an adapter-based fine-tuning method tailored for an aviation foundation model. The proposed ARS-Adapter comprises a standard Adapter

module coupled with an additional depthwise convolution module, shown as Fig.12. The latter is specifically designed to enhance the model's performance in tasks such as detection and tracking. Like AdaptFormer [55], the introduced ARS-Adapter module operates in parallel with the model. The Adapter module featuring the depthwise convolution is paralleled with the MLP layer, while the Adapter module without this convolution module is paralleled with the Attention layer. Therefore, the forward propagation is:

$$\text{Adapter-MSA} = \text{Up}(\text{GELU}(\text{Down}(x))) \quad (17a)$$

$$\text{Adapter-FFN} = \text{Up}(\text{GELU}(\text{Conv}(\text{GELU}(\text{Down}(x))))) \quad (17b)$$

Specifically, the downsampling layer performs 16 times downsampling in the embedding dimension, and the corresponding upsampling layer performs 16 times upsampling. In parallel with FFN, the adapter introduces an additional convolution layer, which uses 7×7 depth-separated convolution to reduce fine-tuning parameters while introducing more spatial information.

During training, the parameters of the entire pre-trained model will be frozen, and only the parameters of the ARS-Adapter mentioned above module will be trained and updated. This approach allows the pre-trained model to achieve the same effect as full fine-tuning by only fine-tuning less than 0.5% of the parameters. The specific experimental results are detailed in Sec.5.3.2.

5 EXPERIMENTS

5.1 Pre-training Implementation

In the pre-training phase of our model, approximately 5.4 million image patches, as mentioned earlier, are utilized. Before pre-training, we initialize the model parameters using Kaiming initialization. Subsequently, we perform 100 epochs of masked image modeling (MIM) pre-training. During MIM pre-training, the input image size is 224, and random cropping and scaling are applied to the input images. The mask size is set to 32 pixels. The batch size is 2048,

TABLE 2
Semantic Segmentation: Comp. on UDD6

Methods	Other		Facade		Road		Vegetation		Vehicle		Roof		mAcc	mIoU
	Acc	IoU												
DeeplabV3+ [42]	92.6	81.8	88.6	72.3	85.3	71.2	83.6	70.8	78.9	62.9	92.4	80.2	86.9	73.2
DANet [43]	92.8	82.1	89.3	72.6	84.5	71.3	81.8	71.6	82.6	63.1	93.8	81.3	87.5	73.7
ACNet [44]	93.1	82.8	90.1	73.2	84.8	71.5	81.6	71.2	83.2	64.2	94.2	81.8	87.8	74.1
OCRNet [45]	92.7	81.9	90.2	73.4	84.3	71	81.9	71.8	83	63.6	94	81.6	87.7	73.9
SETR [46]	91.8	79.6	88.3	70.9	82.6	69.8	81.6	69.6	77.8	61.8	90.8	79.9	85.5	71.9
Segformer [47]	93	82.5	88.9	73.1	86.2	72.3	89.3	71.8	80.1	68.6	91.6	80.8	88.1	74.9
C-Swin [48]	94.2	84.8	89.8	74.9	88.5	73.8	86.3	73.6	83.2	64.9	95.6	86.9	89.6	76.5
UAVFormer [49]	95.2	86.9	90.3	78.3	89.6	75.6	88.1	74.8	82.3	65.6	96.3	84.6	90.3	77.6
RingMo(U) [1]	91	80.4	89.4	74.6	85.5	73.2	89.6	78.4	77.8	62.3	91.1	82.9	87.4	75.3
RingMo-Aerial(U)	90.4	81.1	89.7	77.1	88.7	77.4	90.4	80.2	81.3	68.9	95.9	86.3	89.4	78.5
RingMo-Aerial(M)	90.7	80.9	90.2	77.4	88.4	77.1	90.5	80.8	82.1	69.4	96.3	87.8	89.7	78.9

TABLE 3
Semantic Segmentation: Comp. on Floodnet

Methods	Building		Road		Water	Tree	Vehicle	Pool	Grass	OA	mIoU
	Flooded IoU	Non-Flooded IoU	Flooded IoU	Non-Flooded IoU							
SegNet [56]	44.72	69.85	39.70	76.44	71.17	76.88	32.74	35.87	85.84	87.98	59.25
FCN8s [57]	48.93	73.84	43.11	80.22	71.71	77.33	38.19	45.25	86.85	88.78	62.83
FCN16s [57]	44.97	67.54	34.14	72.80	65.39	76.07	34.28	32.27	85.66	87.23	57.01
PSPNet [58]	45.24	70.30	43.05	76.06	74.32	74.59	24.41	40.74	85.88	88.01	59.40
DeepLabV3 [59]	50.32	78.02	48.46	82.06	76.94	79.90	47.14	48.45	88.10	90.13	66.60
DeepLabV3+ [42]	47.62	74.46	43.12	79.07	68.35	76.36	35.47	36.69	85.60	87.79	60.75
UNet [60]	49.95	77.58	43.90	81.90	73.46	78.88	43.30	49.30	87.54	89.56	65.09
HRNet [61]	50.04	79.23	48.62	81.59	75.05	80.16	49.80	50.89	88.38	90.17	67.08
TransUNet [62]	48.97	73.67	43.11	79.09	72.86	77.75	26.27	35.02	86.47	88.82	60.36
RingMo(U) [1]	71.95	66.80	44.22	74.24	61.97	77.97	23.11	33.01	85.22	88.46	59.83
RingMo-Aerial(U)	74.48	77.06	55.78	83.00	70.35	81.41	53.96	58.08	87.04	90.40	71.24
RingMo-Aerial(M)	76.17	77.90	48.57	82.62	62.75	81.70	63.16	65.79	87.16	90.43	71.76

with a base learning rate of 2e-4, a cosine annealing learning rate schedule, and a warm-up period of 2 epochs. Following MIM pre-training, we continue with contrastive learning (CL) pre-training, jointly training for 36 epochs. The input image size remains 224, and similar random cropping and scaling are applied. The batch size is adjusted to 1024, with a base learning rate of 2e-4, a cosine annealing learning rate schedule, and a warm-up period of 1 epoch.

5.2 Performance on Single/Multi-modal Downstream Tasks

We validated the performance of RingMo-Aerial across six downstream tasks, covering both single-modal and multi-modal tasks, and involving a variety of data modalities and tasks commonly encountered in remote sensing scenarios. Detailed descriptions of the datasets, experimental setups, and additional visualizations for each task are provided in the Appendix.

5.2.1 Semantic Segmentation

Comparative results on the UAVID, UDD6, and FloodNet datasets are presented in Tabs. 1, 2, and 3, respectively. The combination of RingMo-Aerial with Mask2Former achieves segmentation outcomes that significantly outperform those of other methods.

Furthermore, we present the qualitative results for a selection of methods in different scenarios, which primarily comprise roads, secondary roads, and car parks.

RingMo-Aerial consistently produces superior segmentation maps. Among these methods, the RingMo-Aerial approach demonstrates excellent segmentation accuracy and the ability to recognize small targets effectively when combining different architectures. In particular, the RingMo-Aerial + UperNet + ARS-Adapter and RingMo-Aerial + Mask2Former methods demonstrate higher accuracy and clarity in the segmentation of small targets (e.g., stationary and moving vehicles), with enhanced boundary and detail capture. This illustrates the significant advantages of our method in complex urban scenes and diverse object classes.

5.2.2 Object Detection

An analysis of all tables reveals that the detection algorithms based on the proposed method as a pre-trained model have achieved state-of-the-art (SOTA) performance. On unimodal datasets such as VisDrone-DET (as shown in Tab.4) and UAVDT (as shown in Tab.5), RingMo-Aerial combined with DDQ DETR (RingMo-Aerial(D)) significantly outperforms other methods. The experimental results further demonstrate that RingMo-Aerial, compared to Swin-Base in Cascade RCNN and DDQ DETR, is a more suitable foundational model for UAV-based object detection tasks.

What's more, RingMo-Aerial(C) exhibits the best performance in small object detection (mAP_s) on the Ship-Dataset, which primarily targets small vessels (as shown in Tab.6), and PP-PicoDet-L follows. In contrast, YOLOX-L and YOLOX-Tiny show the worst results. Notably, RingMo-Aerial(C) consistently excels in small object detection across

TABLE 4
Object Detection: Comp. on VisDrone-DET

Methods	Backbone	mAP	mAP ₅₀	mAP ₇₅
Light-RCNN [63]	ResNet-50	16.5	32.8	15.1
CornerNet [64]	ResNet-50	17.4	34.1	15.8
RetinaNet [65]	ResNet-50	11.8	21.4	11.6
RetinaNet [65]	Swin-Base	22.6	38.1	23.5
YOLOv4 [66]	CSPDarknet-53	-	38.7	
Cascade R-CNN [67]	ResNet-50	16.1	31.9	15.0
Cascade R-CNN [67]	Swin-Base	28.4	45.2	30.1
CEASC [68]	ResNet-18	28.7	50.7	28.4
SOD-YOLOv7 [69]	-	-	53.2	
MFSSODNet [70]	-	-	45.5	
GLSAN [71]	ResNet-50	25.8	51.5	22.9
QueryDet [17]	ResNet-50	28.3	48.1	28.7
VistrongerDet [72]	ResNet-50	33.9	57.3	
DMNet [73]	ResNet-101	29.4	49.3	30.6
HRDNet [74]	ResNet-101	28.3	49.2	28.1
ClusDet [75]	ResNet-101	26.7	50.4	
ClusDet [75]	ResNeXt-101	28.4	53.2	
SDPDet [76]	ResNet-101	34.2	57.8	34.9
AMRNet [77]	ResNet-101	31.7	52.6	33.0
OGMN [11]	ResNeXt-101	35.0	59.7	35.8
DDQ-DETR [78]	Swin-Base	36.1	57.1	37.2
RingMo-Aerial (C) *	RingMo-Aerial	31.1	51.8	32.5
RingMo-Aerial (A) *	RingMo-Aerial	31.0	51.4	32.1
RingMo-Aerial (D) *	RingMo-Aerial	38.6	63.3	39.4

* RingMo-Aerial (C), (A), (D) represent the RingMo aerial backbone with Cascade RCNN detection algorithm, ARS-Adapter and Cascade RCNN algorithm, and DDQ DETR algorithm. Same below.

TABLE 5
Object Detection: Comp. on UAVDT

Methods	Backbone	mAP	mAP ₅₀	mAP ₇₅
GLSAN [71]	ResNet-50	17.0	28.1	18.8
DMNet [73]	ResNet-50	14.7	24.6	16.3
ClusDet [75]	ResNet-50	13.7	26.5	12.5
AMRNet [77]	ResNet-50	18.2	30.4	19.8
DSHNet [79]	ResNet-50	17.8	30.4	19.7
EfficientDet [80]	Efficient-B7	13.1	31.8	10.9
YOLOv4 [66]	CSPDarknet-53	13.4	30.6	11.3
SDPDet [76]	ResNet-50	20.0	32.0	23.1
QueryDet [17]	ResNet-50	14.3	27.2	16.6
Cascade R-CNN [67]	Swin-Base	19.0	31.4	19.2
OGMN [11]	ResNet-50	20.9	34.5	23.2
OGMN [11]	ResNet-101	24.2	39.9	26.8
RingMo-Aerial (C)	RingMo-Aerial	21.4	33.1	21.9
RingMo-Aerial (D)	RingMo-Aerial	25.2	39.9	27.1

all tasks, further validating its superiority in complex scenarios.

For the multimodal dataset, DroneVehicle (as shown in Tab.7), RingMo-Aerial (C) achieves the best performance in the RGB+IR modality with an mAP₅₀ of 71.6, significantly outperforming other methods. Although methods like Dual-YOLO and CIAN(OBB) also show strong performance in the RGB+IR modality, they still fall short compared to RingMo-Aerial. This indicates that RingMo-Aerial holds significant advantages in handling cross-modality object detection tasks, particularly in UAV image applications. Additionally, the outstanding performance of RingMo-Aerial in multimodal scenarios further validates its effectiveness as a general pre-trained model, particularly in providing higher accuracy and robustness in object detection tasks across diverse and complex environments.

In the domain of Synthetic Aperture Radar (SAR)

TABLE 6
Object Detection: Comp. on ShipDataset

Methods	Backbone	mAP	mAP ₅₀	mAP _s
RetinaNet [65]	RetinaNet	76.0	98.6	40.4
UAV-YOLO [81]	DarkNet-53	86.3	99.5	-
TPH-YOLOv5 [82]	CSPDarknet53+SPP	89.6	99.2	-
YOLOv7 [83]	EfficientNet-B0	88.7	99.6	-
NanoDet-Plus [84]	MobileNetV2	83.1	96.4	41.8
YOLOX-L [85]	CSPDarkNet-53	68.5	93.5	27.6
Center-Net++ [86]	ResNet-101	88.8	99.0	70.8
YOLOX-Tiny [85]	CSPDarkNet-53	71.1	96.4	30.1
PP-PicoDet-L [87]	ESNet	89.7	98.9	67.3
Cascade R-CNN [67]	Swin-Base	88.3	99.0	62.6
RingMo-Aerial(C)	RingMo-Aerial	83.7	99.1	72.3

TABLE 7
Object Detection: Comp. on DroneVehicle

Methods	Modality	Backbone	mAP ₅₀
Faster R-CNN(OBB) [88]	RGB	ResNet101	44.6
RoITransformer [89]	RGB	ResNet101	47.9
YOLOv7 [83]	RGB	EfficientNet-B0	68.5
S ² ANet [90]	RGB	RetinaNet	57.3
Oriented R-CNN [91]	RGB	ResNet101	62.3
Cascade R-CNN [67]	RGB	Swin-Base	69.5
Faster R-CNN(OBB) [88]	IR	ResNet101	44.6
RoITransformer [89]	IR	ResNet101	59.2
YOLOv7 [83]	IR	EfficientNet-B0	66.7
S ² ANet [90]	IR	RetinaNet	64.8
Oriented R-CNN [91]	IR	ResNet101	65.5
Cascade R-CNN [67]	IR	Swin-Base	69.8
UA-CMDet [92]	RGB+IR	EfficientNet-B0	64.0
Halfway Fusion(OBB) [93]	RGB+IR	Halfway Fusion	68.2
CIAN(OBB) [94]	RGB+IR	VGG16	70.2
Dual-YOLO [95]	RGB+IR	Dual-YOLO	71.5
Cascade R-CNN [67]	RGB+IR	Swin-Base	69.8
RingMo-Aerial(C)	RGB+IR	RingMo-Aerial	71.6

datasets (as shown in Tab.8), the RingMo-Aerial backbone network, integrated with various detection algorithms such as Cascade R-CNN, and the proposed ARS-Adapter, has demonstrated a notable enhancement in performance. Mainly, the RingMo-Aerial(C) configuration has achieved an mAP of 36.2% and a mAP₅₀ of 84.4%, highlighting its superiority in SAR modality. These results substantiate the efficacy of the RingMo-Aerial backbone in processing SAR imagery. Furthermore, the performance of RingMo-Aerial on multimodal datasets reinforces its viability as a universal pre-trained model, especially in enhancing precision and robustness for object detection tasks across diverse and intricate environments. These findings underscore the potential application value of RingMo-Aerial in the field of remote sensing, specifically for aerial object detection tasks utilizing SAR data.

Additionally, we present the qualitative results of several methods across different scenarios, primarily focusing on roads and sports fields. For optical images, as shown in the appendix, the RingMo-Aerial detection model demonstrates superior performance, particularly in detecting small-scale targets. In the sports field scenario, RingMo-Aerial effectively identifies distant groups of people, even those not annotated in the test set, while RingMo fails to detect these groups. Similarly, RingMo-Aerial accurately detects distant vehicles in road scenarios, whereas RingMo underperforms.

TABLE 8
Object Detection: Comp. on AerialSARDData

Methods	Backbone	mAP	mAP ₅₀
RetinaNet [65]	RetinaNet	22.9	64.3
Cascade R-CNN [67]	ResNet101	34.5	81.3
RingMo-Aerial(A) *	RingMo-Aerial	30.9	77.6
RingMo-Aerial(C) *	RingMo-Aerial	34.9	82.6

* RingMo-Aerial (A), (C) represent the RingMo-Aerial backbone with ARS-Adapter and Cascade RCNN algorithm.

RingMo-Aerial also demonstrates outstanding small target recognition capabilities for SAR and IR images. As shown in the appendix, RingMo tends to misclassify densely overlapping vehicles at the end of the road, while RingMo-Aerial maintains a high level of class confidence. The visualized results confirm the model's excellent performance on multi-modal data, including optical, SAR, and IR images. RingMo-Aerial's exceptional performance across multiple modalities proves its strong generalization ability and highlights its great potential as the first foundational model for ARS.

5.2.3 Scene Classification

TABLE 9
Scene Classification: Comp. on AID and RESISC-45

Model	AID (OA) (TR=20%/50%)	RESISC-45 (OA) (TR=10%/20%)
GASSL [96]	93.55/95.92	90.86/93.06
SeCo [33]	93.47/95.99	89.64/92.91
SatMAE [97]	95.02/96.94	91.72/94.10
RingMo [1]	96.90/98.34	94.25/95.67
RVSA [98]	97.03/98.50	93.93/95.69
DINO-MC [99]	95.16/97.09	-
TOV [100]	95.16/97.09	90.97/93.79
SSL4EO [101]	91.06/94.74	87.60/91.27
CMID [102]	96.11/97.79	91.84/94.07
CACo [103]	90.88/95.05	88.28/91.94
CROMA [104]	96.44/97.58	92.63/95.04
SatLas [105]	94.96/97.38	92.16/94.70
GFM [106]	95.47/97.09	-
Scale-MAE [107]	96.44/97.58	92.63/95.04
SkySense [2]	97.68/98.60	94.85/96.32
RingMo [1]	96.90/98.34	94.25/95.67
RingMo-Aerial	95.81/96.46	92.28/95.65

The comparison results are shown in Tab.9. Although RingMo-Aerial does not perform as well as specialized satellite models like SkySense in nadir-view classification, it still demonstrates strong performance, reflecting its robust generalization capability.

5.2.4 Change Detection

The comparison results are shown in Tab.10. RingMo-Aerial combined with BIT can achieve change detection results that far exceed other methods. In a rigorous comparative evaluation against current state-of-the-art technologies, RingMo-Aerial proved its capabilities in the specialized field of remote sensing change detection. When evaluated against LEVIR-CD and CDD datasets, the model demonstrated a clear competitive advantage, highlighting the robustness and effectiveness of the backbone network integrated into our architecture.

TABLE 10
Change Detection: Comp. on LEVIR-CD and CDD

Methods	LEVIR-CD		CDD	
	F1	IoU	F1	IoU
FC-Siam-Di [108]	86.31	83.31	70.61	54.57
FC-Siam-Conc [108]	83.69	76.77	75.11	60.14
IFNet [109]	88.13	82.93	90.30	71.91
STANet [110]	87.30	77.40	84.12	72.22
BIT [111]	89.31	89.37	88.90	80.01
SNUNet [112]	88.16	87.17	83.89	72.11
ChangeFormer [113]	90.40	88.80	89.83	81.53
RingMo [1]	89.53	82.38	90.90	84.09
RingMo-Aerial	92.71	87.10	94.62	90.09

The comparison of visual results on the LEVIR dataset reveals significant differences in the performance of models with different backbones in building detection and segmentation tasks, as shown in the appendix. The RingMo-Aerial model demonstrates superior accuracy, with fewer false positives (red areas) and false negatives (green areas), highlighting its advantages in processing remote sensing images. In contrast, the ResNet18 and Swin-Base models exhibit more false positives and false negatives, particularly in complex building layouts, where RingMo-Aerial shows greater robustness.

RingMo-Aerial's commendable performance not only makes it a key player in the field but also highlights the importance of the impact of foundation model innovation. These elements are critical to pushing the frontiers of remote sensing analysis and setting new benchmarks for future research and applications.

5.2.5 3D-Reconstruction

Tab.11 provides a performance comparison of our method and other methods on the LuoJia-MVS and WHU datasets. Obviously, under the premise of taking five views as input, our method achieves the best estimation performance and the lowest prediction error. On the LuoJia-MVS dataset, our method achieves an MAE error of 0.122m, 98.1% and 96.5% of <0.6m and <3-interval accuracy, which is better than the existing advanced method Cas-MVSNet. It improves MAE, <0.6m, <3-interval by 13.5% (0.122 vs. 0.141), 0.2% (98.1% vs. 97.9%) and 1.1% (96.5% vs. 95.4%), respectively, which is a significant improvement. In addition, on the WHU dataset, our method surpasses the advanced method Cas-MVSNet and achieves an MAE error of 0.091m, a <0.6m accuracy of 98.0% and a <3-interval accuracy of 97.9%. It can be seen that our proposed method also has superior generalization performance in multi-view stereo reconstruction methods.

5.2.6 Object Tracking

The comparison results on the VisDrone-MOT dataset are shown in Tab.12. RingMo-Aerial can achieve the best tracking results, far exceeding other methods. In the AIR-MOT dataset (as shown in Tab.13), which contains more small aircraft and boat targets, RingMo-Aerial achieved a MOTA of 68.6 and an IDF1 of 81.3, though slightly trailing behind CFTrack. Meanwhile, in the AIR-HSAO dataset (as shown in Tab.14), RingMo-Aerial maintained its robust performance with a MOTA of 60.7 and an IDF1 of 74.4, approaching the best-performing methods. Overall, the RingMo-Aerial algorithm exhibited excellent multi-object tracking capabilities

TABLE 11
3D-Reconstruction: Comp. on LuoJia-MVS and WHU

Number of Views	Model	MAE	LuoJia-MVS		WHU		
			<0.6m	<3-interval	MAE	<0.6m	<3-interval
Three views *	PatchmatchNet [114]	0.252	92.7	87.2	0.173	96.5	94.8
	Fast-MVSNet [115]	0.194	95.7	92.0	0.184	95.5	94.1
	MVSNet [116]	0.172	96.1	92.4	0.190	95.0	94.3
	R-MVSNet [117]	0.177	96.0	93.5	0.183	95.3	93.5
	RED-Net [118]	0.109	98.2	96.9	0.112	98.1	97.9
	Cas-MVSNet [119]	0.103	98.4	97.1	0.111	97.7	97.6
	RingMo-Aerial	0.095	98.7	97.8	0.121	97.8	97.5
Five views *	PatchmatchNet [114]	0.283	90.4	84.1	0.160	96.9	95.0
	Fast-MVSNet [115]	0.357	84.6	74.9	0.157	96.1	95.6
	MVSNet [116]	0.270	91.2	81.8	0.160	95.8	95.5
	R-MVSNet [117]	0.259	92.3	86.7	0.173	95.4	93.8
	RED-Net [118]	0.156	94.9	90.5	0.104	98.1	97.9
	Cas-MVSNet [119]	0.141	97.9	95.4	0.095	97.8	97.8
	RingMo-Aerial	0.122	98.1	96.5	0.091	98.0	97.9

* 'Three Views' and 'Five Views' represent the number of views for the network's input is three and five, respectively.

TABLE 12
Object Tracking: Comp. on Visdrone-MOT

Methods	MOTA	IDF1
SiamMOT [120]	31.9	48.3
ByteTrack [121]	35.7	37.0
UAVMOT [122]	36.1	51.0
OCSORT [123]	39.0	50.4
MOTR [124]	22.8	41.4
TrackFormer [125]	24.0	30.5
FOLT [126]	42.1	56.9
U2MOT [127]	52.3	69.0
RingMo [1]	48.4	63.1
RingMo-Aerial	52.6	67.8

TABLE 13
Object Tracking: Comp. on AIR-MOT

Methods	MOTA	IDF1
CKDNet+SMTNet [128]	64.2	64.9
ByteTrack [121]	56.1	73.5
OCSORT [129]	35.6	53.8
StrongSORT [130]	36.1	54.1
CenterTrack [131]	66.3	79.3
TGram [132]	65.7	66.8
RSMOT [133]	67.0	80.4
CFTTrack [134]	70.8	82.7
RingMo-Aerial	68.6	81.3

in these complex scenarios, coming close to or surpassing the state-of-the-art methods in several key metrics.

Furthermore, the visualization results of the AIR-MOT sequences demonstrate the tracking performance of the RingMo-Aerial method in four selected video sequences, particularly in complex and dynamic scenarios. The clarity and precision of the bounding boxes further highlight the method's effectiveness in distinguishing and tracking various objects under different environmental conditions. This visualization provides qualitative solid evidence of the proposed algorithm's performance in handling multi-object tracking tasks in ARS videos.

TABLE 14
Object Tracking: Comp. on AIR-HSAO

Methods	MOTA	IDF1
TraDeS [135]	59.6	75.1
CenterTrack [131]	60.3	74.5
DSFNet [136]	60.2	75.8
FairMOT [137]	54.8	71.3
CTracker [138]	51.1	65.1
ByteTrack [121]	60.3	74.5
MGTrack [139]	63.5	77.4
RingMo-Aerial	60.7	74.4

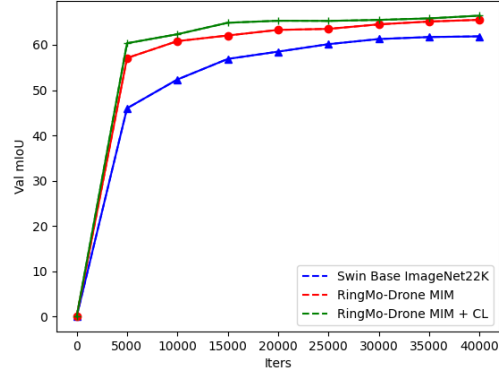


Fig. 13. The ablation experiment on the UAVID dataset and UperNet is used as the segmentation head. RingMo-Aerial pretrained with MIM and CL achieves the fastest convergence speed and optimal segmentation performance.

5.3 Ablation Experiments

5.3.1 Ablation Experiments on pre-training

We utilize UperNet model on UAVID and Cascade RCNN model on Visdrone-DET. The comparative analysis involves three foundation models: the Swin Transformer Base model pre-trained on ImageNet22K [22], the RingMo-Aerial model solely pre-trained with MIM, and the RingMo-Aerial model pre-trained with both MIM and CL. This comparative investigation aims to substantiate the efficacy and consistency of

TABLE 15
Ablation Experiments

	UAVID		Visdrone-DET	
	mAcc	mIoU	mAP	mAP ₅₀
RingMo	71.6	61.9	28.4	45.2
RingMo-Aerial (MIM)	75.7	65.8	30.5	50.3
RingMo-Aerial (MIM + CL)	76.5	66.4	31.1	51.8

TABLE 16
Ablation Experiments with the proposed ARS-Adapter

	UAVID		Visdrone-DET	
	mAcc	mIoU	mAP	mAP ₅₀
RingMo-Aerial (MIM)	71.6	62.9	25.3	42.7
RingMo-Aerial (MIM + CL)	74.3	64.4	31.0	51.4

the proposed method.

The comparison is shown in Fig.13 and Tab.15. The experimental findings reveal a progressive convergence speed and performance enhancement across the three foundation models. Notably, the RingMo-Aerial model trained with MIM and CL exhibits the swiftest convergence and attains the optimal performance. This observation underscores the synergistic relationship between the FE-MSA module proposed in this study and the MIM + CL pre-training strategy, affirming their mutually reinforcing nature and consistent effectiveness.

In addition, models pretrained with MIM combined with CL exhibit enhanced adaptability when used with ARS-Adapter. Consequently, ablation studies were conducted to compare ARS-Adapter between models solely pretrained with MIM and those pretrained with both MIM and CL. Comparative results on the UAVID and VisDrone-DET datasets are presented in Tab.16. The experimental findings indicate that models additionally trained with CL significantly improve performance in both detection and segmentation tasks when fine-tuned with ARS-Adapter.

5.3.2 Performance Comparison Between ARS-Adapter and Other Fine-Tuning Methods

In the context of ARS, traditional model fine-tuning presents specific challenges. These include the propensity for overfitting due to the extensive pre-training on diverse tasks, which can lead to a model that is overly tailored to the nuances of the training data, thereby compromising its applicability to new, unseen data. Overfitting is particularly problematic in ARS, where models are not only expected to generalize across various tasks but also to adapt to the unique perspectives and resolutions inherent in aerial imagery. This contrasts with ApRS, which typically operates within a more constrained perspective and resolution, reducing the risk of overfitting to specific views. The ARS-Adapter, therefore, addresses these challenges by introducing a parameter-efficient fine-tuning approach that minimizes overfitting risks while maintaining high performance, as evidenced by the experimental results.

This section compares ARS-Adapter against other fine-tuning methods, using UAVID and VisDrone-DET datasets with UperNet and Cascade RCNN as the segmentation and detection frameworks, respectively. The aim is to assess

TABLE 17
Comp. between fine-tuning methods

Methods	Parameters	UAVID		VisDrone-DET	
		mAcc	mIoU	mAP	mAP ₅₀
Frozezn	0%	61.2	49.3	21.5	36.2
Full	100%	76.5	66.4	31.1	51.8
Adapter	0.39%	68.9	57.7	28.9	49.1
AdaptFormer	0.39%	71.3	62.1	30.3	50.8
ARS-Adapter *	0.41%	74.3	64.4	31.0	51.4

* Although ARS-Adapter is less accurate than global fine-tuning, it significantly outperforms other fine-tuning methods when the proportion of fine-tuning parameters is almost constant.

the effectiveness of ARS-Adapter compared to conventional fine-tuning techniques.

The experimental results are presented in Tab.17. For clarity, we compare ARS-Adapter with full fine-tuning, zero fine-tuning, and two other fine-tuning methods (Adapter and AdaptFormer). Full fine-tuning is a performance upper bound, while zero fine-tuning provides a reference for minimal parameter adjustment. ARS-Adapter requires a similar proportion of parameters(0.41%) to be adjusted as Adapter(0.39%) and AdaptFormer(0.39%), but achieves superior fine-tuning efficiency. Additionally, the performance loss compared to full fine-tuning(100%) is limited to approximately 2%, demonstrating that ARS-Adapter can achieve high performance with minimal parameter adjustments.

These results indicate that ARS-Adapter maintains high performance while significantly reducing the number of parameters requiring adjustment, demonstrating its efficiency in fine-tuning.

6 CONCLUSION

The RingMo-Aerial model presented in this paper represents the first large foundation model specifically tailored for Aerial Remote Sensing (ARS) vision tasks. Following an in-depth analysis of the unique aspects of ARS vision tasks, this study identified the necessity for foundation model research in this domain and proposed a series of innovative solutions based on the RingMo framework to address the specific challenges therein. Our experiments demonstrate that the RingMo-Aerial model achieves SOTA performance across various datasets for ARS vision tasks. This demonstrates the utility and effectiveness of our approach in improving ARS vision tasks. In the future, RingMo-Aerial and its associated technologies are poised to provide a robust foundation model for ARS vision research. Future work will focus on improving the model's generalization capabilities, computational efficiency, and broader real-world deployment. Additionally, we will explore the extension of the RingMo-Aerial model to other vision tasks and scenarios, aiming to expand its application scope.

APPENDIX A

SEMANTIC SEGMENTATION

A.1 Datasets and Evaluation Metrics

For semantic segmentation, the UAVID [140], UDD6 [141] and FloodNet [142] datasets are employed.

- **UAVID.** The UAVID dataset has 42 sequences of 4K resolution in total (20 train, 7 valid, and 15 test), and each sequence contains ten pictures. In the experiment, all images were cropped into 1024×1024 pixel slices with 256 pixels of overlap. A total of 27 sequences in the training and validation sets are used for training, and 15 sequences in the test set are used for testing.
- **UDD6.** The training set of the UDD6 dataset includes 106 images, and the validation set includes 35 images. All of the images are 4K resolution. In the experiment, all images were cropped into 1024×1024 pixel slices with 256 pixels of overlap. The training set is used for training, and the validation set is used for testing.
- **FloodNet.** The FloodNet dataset contains 500 high-resolution remote sensing images with a resolution of 4K. The dataset is divided into training, validation, and test sets, with the training set containing 300 images, the validation set containing 100 images, and the test set containing 100 images. Images are annotated as flood and non-flood areas, supporting multi-class flood impact assessment. All images are cropped into 1024×1024 pixel slices with a 256-pixel overlap in the experiment, facilitating the training and evaluation of machine learning models.

In our experiment of semantic segmentation, the evaluation metrics are mean intersection over union (**mIoU**), mean accuracy (**mAcc**), and average accuracy (**aAcc**).

A.2 Experiment Settings

The experiment of the semantic segmentation is based on segmentation [143], UperNet [144], and Mask2Former [145] are employed as the segmentation framework. The training process spanned a total of 40,000 iterations with a batch size of 8 total (2 per GPU and 4 NVIDIA A40 GPU are used). The AdamW [146] optimizer is utilized for the optimization, and the base learning rate is set to 0.0001, accompanied by a weight decay of 0.05. In addition, the Poly learning rate strategy is used for learning rate scheduling, and the final learning rate drops to 0.

APPENDIX B

OBJECT DETECTION

B.1 Datasets and Evaluation Metrics

To conduct a comprehensive comparison of object detection methods, we selected four unimodal benchmark datasets, including the VisDrone-DET [147], UAVDT [148] and ShipDataset [149], as well as one multimodal benchmark dataset, DroneVehicle [92] and our collection of SAR airborne remote sensing data, to demonstrate the performance of the representative methods discussed in this paper.

- **VisDrone-DET.** The Visdrone-DET dataset is the detection task part of the VisDrone dataset. The resolution of the images is about 2k. The RingMo-Aerial experiment

crops the original image to 640×640 and uses multi-scale cropping and resizing for enhancement. The training set and validation set are used for training, and the labeled test-dev set is used for testing.

- **UAVDT.** The UAVDT dataset is another popular ARS detection dataset, containing 23,258 images for training and 15,069 images for testing with an average resolution of 1080×540 pixels. The RingMo-Aerial experiment uses multi-scale cropping and resizing for enhancement.
- **ShipDataset.** The ShipDataset, captured at a resolution of 3840×2160 , encompasses five distinct scenarios in Shanghai, China, characterized by varying shooting angles and lighting conditions. This dataset has 96.97% small ships. The images within this dataset predominantly feature congested ship traffic. The RingMo-Aerial experiment uses multi-scale resizing for enhancement.
- **DroneVehicle.** The DroneVehicle dataset is a large-scale dataset specifically designed for drone-based RGB-Infrared cross-modality vehicle detection tasks. It includes 28,439 pairs of RGB-Infrared images, totaling 56,878 images, covering various urban scenarios such as roads, residential areas, and parking lots under different lighting conditions, including day, night, and dark night. The RingMo-Aerial experiment uses multi-scale cropping and resizing for enhancement.
- **AerialSARDATA.** To evaluate the performance of our foundational model across various modalities, we employed a hexacopter drone (1800 Pro) equipped with a miniature Synthetic Aperture Radar (MS-102) mounted on its underside. This setup was utilized to collect a dataset of SAR-based aerial remote sensing for vehicle detection. The dataset comprises a total of 711 images, with the training set consisting of 536 images and the test set comprising 175 images, all at a resolution of 800×800 pixels. The images encompass a diverse range of scenarios, including airports, roads, and residential areas.

In our object detection experiments, the evaluation metrics employed are mean average precision (**mAP**), mAP at an IoU threshold of 50 (**mAP₅₀**), and mAP at an IoU threshold of 75 (**mAP₇₅**). For datasets containing smaller objects, we also utilize **mAP_s**, which represents the mean average precision for detecting small objects (with pixels smaller than 32×32).

B.2 Experiment Settings

The experiment of the object detection is based on mmdection [150], Cascade RCNN [67] and DDQ DETR [78] are employed as the detection framework. The training process spanned a total of 12 epochs for Cascade RCNN, with a batch size of 32 total (8 per GPU and 4 NVIDIA A40 GPU are used). For DDQ DETR, 36 epochs were spanned with a batch size of 16 total (4 per GPU and 4 NVIDIA A40 GPU are used). The AdamW [146] optimizer is utilized for the optimization, and the base learning rate is set to 0.0001, accompanied by a weight decay of 0.05. In addition, the learning rate is decreased by 10 after the 8th and 11th epochs

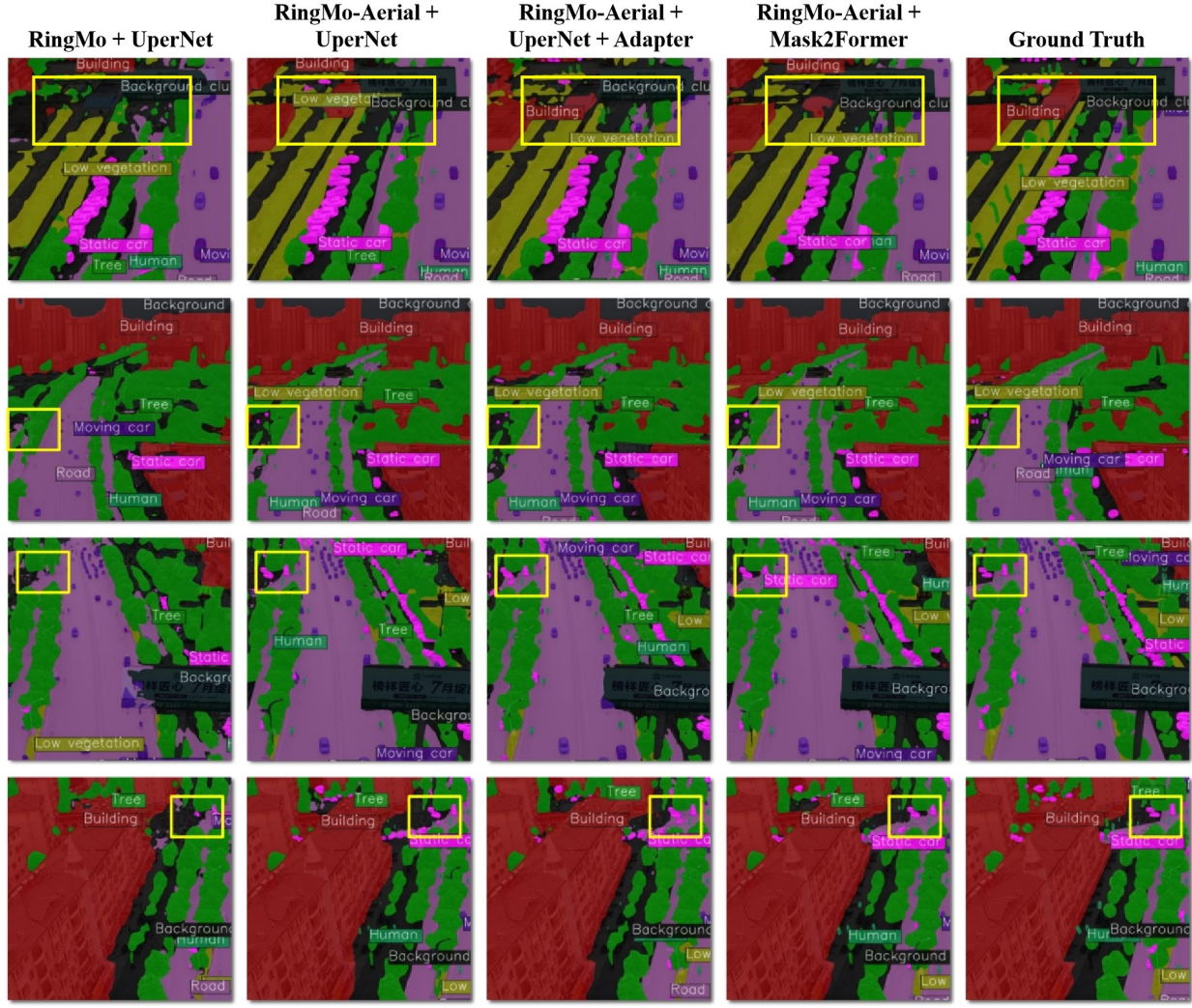


Fig. 14. Qualitative comparison of semantic segmentation results on the UAVID dataset using different methods. The figure illustrates differences in capturing details such as vegetation, moving vehicles, and buildings, with highlighted regions emphasizing variations in detail and performance.

for Cascade RCNN and after the 27th and 33rd epochs for DDQ DETR.

APPENDIX C CHANGE DETECTION

C.1 Datasets and Evaluation Metrics

For semantic segmentation, the LEVIR [110] and CDD [151] datasets are employed.

- **LEVIR.** The LEVIR-CD is a publicly available, extensive remote sensing change detection dataset. It comprises 637 pairs of high-resolution images, each with a dimension of 1024×1024 pixels at a 0.5-meter resolution. Adhering to the standard dataset partitioning, we have processed the original images by extracting non-overlapping patches, each measuring 256×256 pixels. Consequently, this results in a distribution of 7120, 1024, and 2048 image patches allocated for training, validation, and testing phases.
- **CDD.** The CDD dataset is a comprehensive collection of bi-temporal remote sensing imagery, comprising seven

pairs of images with a resolution of 4725×2700 pixels and an additional four pairs with dimensions of 1900×1000 pixels. These images have been meticulously synchronized and cropped to yield 16,000 pairs of 256×256 pixel patches. This curated subset is strategically divided into a training set of 10,000 pairs, a validation set of 3,000 pairs, and a test set of the remaining 3,000 pairs. To enhance the realism and applicability of the trained models, the dataset incorporates seasonal variations, thereby providing a more challenging and convincing foundation for network training.

C.2 Experiment Settings

Our model adopts BIT with Swin Transformer as the backbone. The experiments use overall accuracy (OA) and F1 and IoU scores about change detection as the primary evaluation metrics. The model is trained with an AdamW optimizer with a weight decay of 0.01 and beta values equal to (0.9, 0.999). The LR is $2e-3$ for the LEVIR-CD dataset and linearly decays to 0 until trained for 200 epochs, with a total

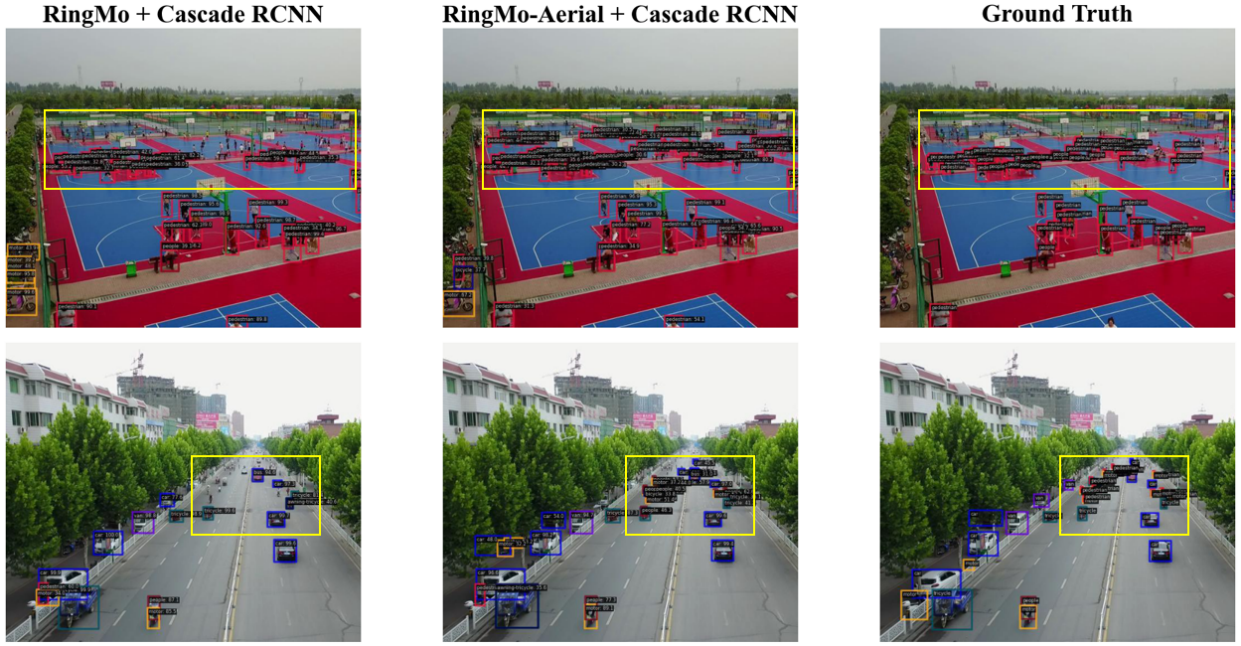


Fig. 15. RingMo-Aerial combined with Cascade RCNN achieves superior detection accuracy compared to the original RingMo model, particularly in complex environments and small object scenarios. It demonstrates reduced false positives and improved bounding box alignment with Ground Truth, highlighting its effectiveness for aerial imagery detection.

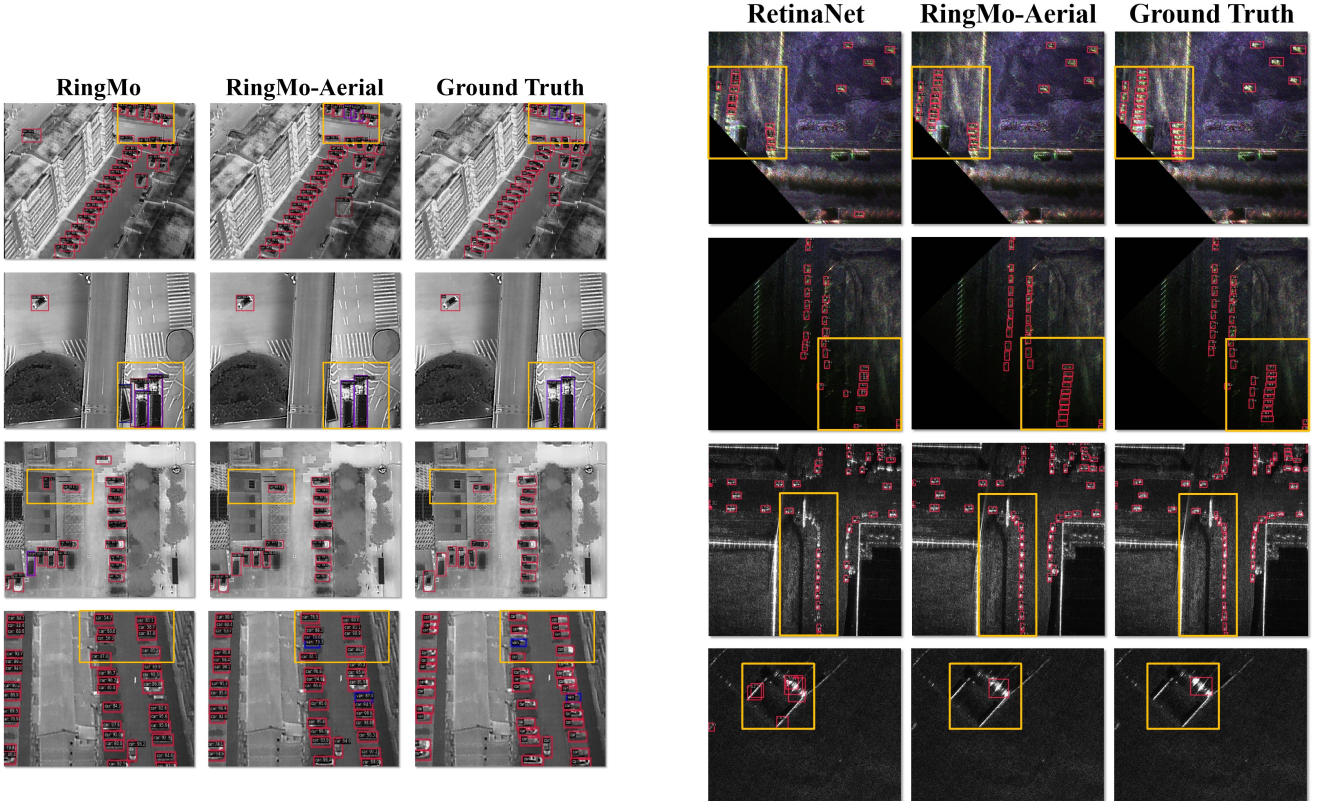


Fig. 16. Qualitative comparison of object detection results on infrared images from the DroneVehicle-IR dataset using different methods. The figure highlights differences in the detection quality of vehicles, road elements, and pedestrian areas, with emphasized regions showcasing variations in accuracy and detail among the compared methods.

Fig. 17. Qualitative comparison of object detection results on the AerialSARData dataset using different methods. The figure highlights differences in detection performance for SAR images, particularly focusing on identifying objects of interest with highlighted regions showing variations in accuracy and detection quality among the methods compared.

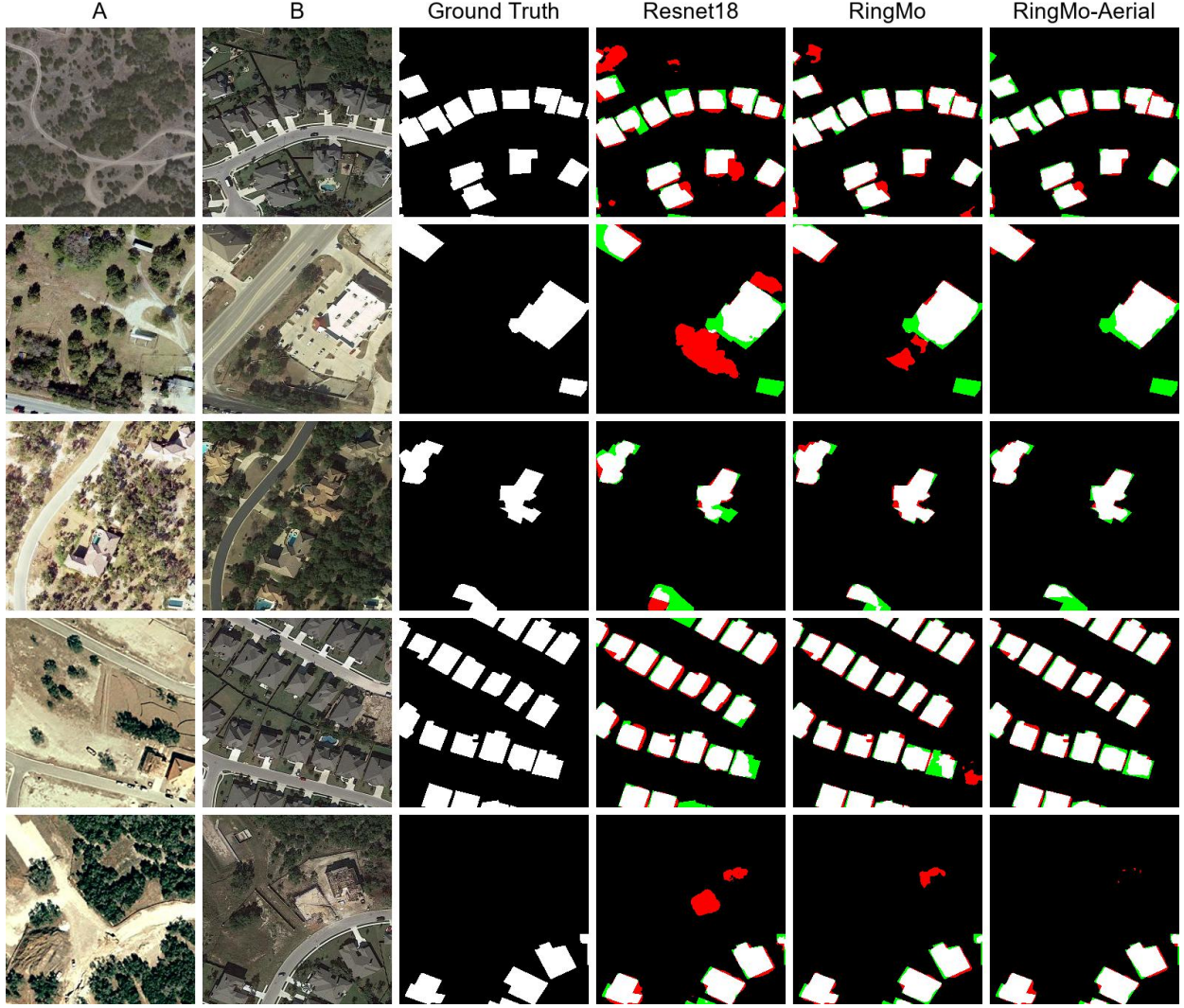


Fig. 18. Comparison of Detection Visualization Results Using Different Backbone Networks with the BIT Algorithm on the LEVIR Dataset. That shows the results of aerial images, where RingMo-Aerial outperforms ResNet18 and RingMo, with fewer false positives and false negatives. RingMo-Aerial closely matches the Ground Truth, demonstrating the best accuracy in change Detection. The black region represents true negative, the white region represents true positive, the green region represents false negative, the red region represents false positive.

batch size 16 for datasets (8 per GPU, using 2 NVIDIA A40 GPUs).

APPENDIX D SCENE CLASSIFICATION

D.1 Datasets and Evaluation Metrics

For scene classification, the AID [152] and RESISC-45 [153] datasets are employed.

- **AID.** The AID dataset is a large-scale data set used to evaluate the performance of aviation scene classification. It contains images collected from Google Earth and covers 30 scenes.
- **NWPU-RESISC45.** The NWPU-RESISC45 dataset is a publicly available Remote Sensing Image Scene Classification (RESISC) benchmark. The dataset contains 31,500 images covering 45 scene classes, with 700 images in each class.

In our experiment of scene classification, the training proportions in the AID dataset were set to TR = 20% and

TR = 50%, respectively. In the NWPU-RESISC dataset, the proportion of training samples was set to TR = 10% and TR = 20%, respectively. The experiments use overall accuracy (OA) as a performance metric, the most commonly used performance metric in scene classification.

D.2 Experiment Settings

The experiment of the scene classification is based on mm-pretrain [154], Cascade RCNN [67] is employed as the classification framework. The training process spanned a total of 300 calendar elements, with a total batch size of 16 for dataset AID (8 per GPU, using 2 NVIDIA A40 GPUs) and 128 for dataset NWPU-RESISC45 (64 per GPU, using 2 NVIDIA A40 GPUs). The AdamW [146] optimizer is utilized for the optimization, and the base learning rate is set to 0.0005, accompanied by a weight decay of 0.05. In addition, the Poly learning rate strategy is used for learning rate scheduling, and the final learning rate drops to 0.

APPENDIX E

3D-RECONSTRUCTION

E.1 Datasets and Evaluation Metrics

For 3D-Reconstruction, the and WHU [118] datasets are employed.

- **WHU.** The WHU dataset is a synthetic aerial dataset designed for large-scale multi-view stereo reconstruction tasks. It was generated from a highly accurate 3D surface model and includes a complete set of aerial images as well as cropped sub-image sets specifically for deep learning applications. The images in the dataset cover an area of approximately 6.7×2.2 square kilometers in Meitan County, Guizhou Province, China, with a ground resolution of 0.1 meters. The WHU dataset provides crucial data support for the study of large-scale Earth surface and urban reconstruction and can be utilized for training and testing multi-view stereo matching algorithms.
- **LuoJia-MVS.** The LuoJia-MVS dataset comprises 7,972 five-view images, each with a spatial resolution of 10 cm, accompanied by pixel-wise depth information and precise camera parameters. These images were generated from a highly accurate digital surface model (DSM) constructed using thousands of stereo aerial images.

During the experiment, we used the WHU dataset [118] and the LuoJia-MVS dataset [155] to verify the effectiveness of our proposed method. WHU dataset [118] is the first large-scale aerial multi-view stereo dataset for remote sensing. It was collected from Meitan, Guizhou, China, and was obtained by taking large-scale photos with a tilted five-eye camera on a drone platform. The area of the entire dataset is approximately $6.7 \times 2.2 \text{ km}^2$, and the image resolution is about 0.1m. In addition, the tilt angle of each camera to the central camera is 40° . The WHU dataset gathers high-rise buildings, mountains, forests, and factory scenes, providing a good benchmark for remote sensing multi-view stereo. LuoJia-MVS [155] dataset is a large-scale multi-view stereo dataset collected from a variety of landform types. It was collected in a part of Baiyun, Guiyang, Guizhou, China. The image size of the entire dataset is 768×384 , and the image resolution is about 0.1m. The data consists of five views and pixel-by-pixel depth labels. Land types cover cultivated land, forest land, industrial areas, residential areas, etc.

E.2 Experiment Settings

Our work is coded based on the PyTorch framework. The proposed method is trained and tested on NVIDIA A40, and the batch size is set to 1. During the training process, our method uses the Adam optimizer [156] for parameter optimization and trains for 24 epochs, where the parameter β_1 is set to 0.9, the parameter β_2 is set to 0.999, and the initial learning rate is 0.001. In addition, our method is consistent with the existing multi-stage networks [119]. First, multi-scale features are learned through a multi-scale feature extractor, and the scales are 1/16, 1/4, and 1 of the input size, respectively. Then, deep optimization is performed through three stages of profound hypotheses, and the number of

hypotheses is 48, 32, and 8, respectively. During the experiment, we use three metrics, mean absolute error (MAE), $<0.6\text{m}$, and <3 -interval, to evaluate the performance of the proposed method.

APPENDIX F

OBJECT TRACKING

F.1 Datasets and Evaluation Metrics

For Object Tracking, the following aerial dataset is employed.

- **VisDrone-MOT.** The VisDrone-MOT [157] dataset consists of 96 sequences, including five classes such as pedestrian, car, van, bus, and truck. The VisDrone-MOT train and val set are used for training, and the test set is used for the test.
- **AIR-MOT.** The AIR-MOT dataset [132], derived from the JiLin-1 satellite, is designed for multi-class multiple object tracking (MOT). It includes two categories: airplanes and ships. The dataset comprises 152 videos, with frame rates ranging from 5 to 10 frames per second, a spatial resolution of 1–1.2 meters, and a pixel resolution of 1920×1080 . The target categories in this dataset move relatively slowly.
- **AIR-HSAO.** The AIR-HSAO dataset [139] is designed for tracking high-speed aerial objects derived from the JiLin-1 satellite. It contains 199 videos, though fewer instances are present due to the rapid movement of these objects. The dataset spans 20 diverse regions, including urban areas, harbors, and airports, offering complex backgrounds that challenge object detection and tracking.

In our experiment of object tracking, Multiple Object Tracking Accuracy (**MOTA**) and Identification Flatness (**IDF1**) are used as evaluation metrics.

F.2 Experiment Settings

In the proposed experiment, object tracking is predicated on the detection model of RingMo-Aerial on VisDrone-DET. Specifically, the detection model trained by RingMo-Aerial will undergo an additional five epochs of training on the VisDrone-MOT dataset, during which the backbone network parameters will be frozen to ensure consistency. The training will be conducted with a batch size of 8, distributed as 2 per GPU across 4 NVIDIA A40 GPUs. Throughout the training phase, original images from the VisDrone-MOT dataset will be processed, and multi-scale augmentation will be accompanied to enhance robustness. Upon completion of training on the VisDrone-MOT dataset, the detection model will be subjected to inference on the VisDrone-MOT test set using the MOT tools provided by mmdetection [150]. Subsequently, the model's multi-object tracking performance will be quantified and analyzed.

ACKNOWLEDGMENTS

This work was supported by the National Nature Science Foundation of China under Grant 62331027 and 62301538.

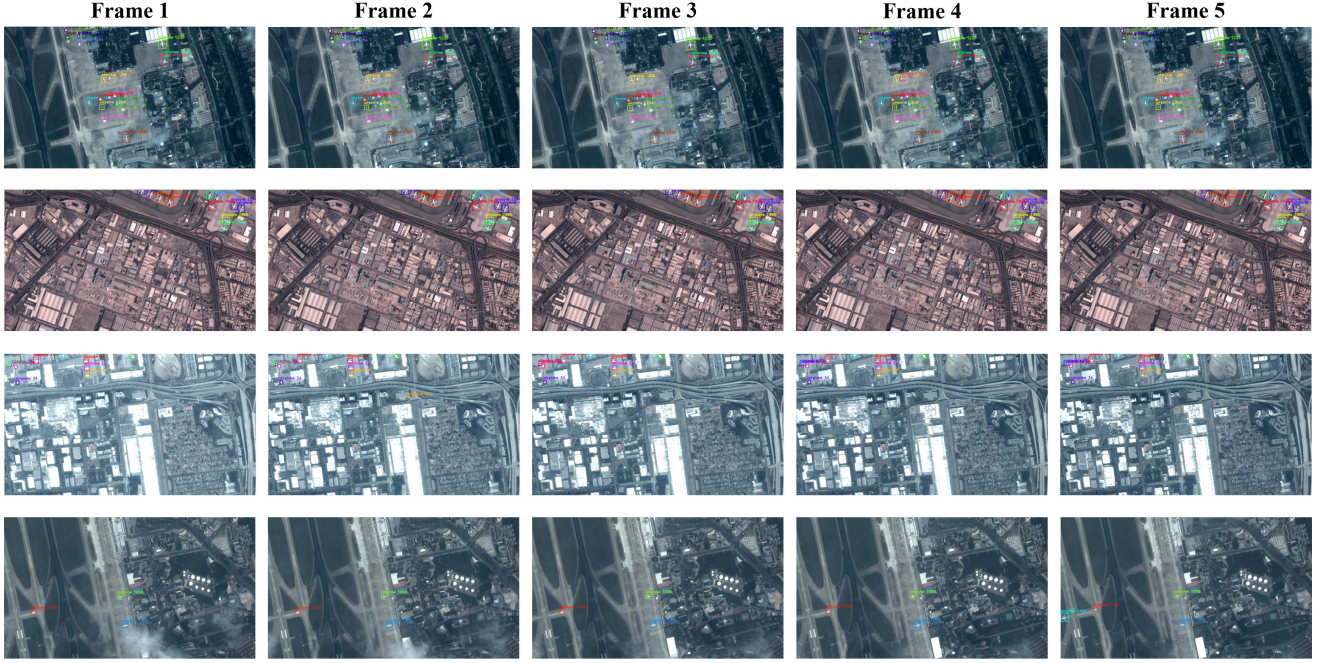


Fig. 19. Qualitative results on the target tracking dataset AIR-MOT using RingMo-Aerial. Four video sequences are selected, where each target is indicated with different colors. The category and target ID are displayed above the bounding boxes, demonstrating RingMo-Aerial's ability to effectively distinguish and track individual targets.

REFERENCES

- [1] X. Sun, P. Wang, W. Lu, Z. Zhu, X. Lu, Q. He, J. Li, X. Rong, Z. Yang, H. Chang, *et al.*, "Ringmo: A remote sensing foundation model with masked image modeling," *IEEE TGRS*, 2022. **2, 4, 9, 10, 12, 13**
- [2] X. Guo, J. Lao, B. Dang, Y. Zhang, L. Yu, L. Ru, L. Zhong, Z. Huang, K. Wu, D. Hu, *et al.*, "Skysense: A multi-modal remote sensing foundation model towards universal interpretation for earth observation imagery," in *CVPR*, pp. 27672–27683, 2024. **2, 4, 12**
- [3] K. He, X. Chen, S. Xie, Y. Li, P. Dollár, and R. Girshick, "Masked autoencoders are scalable vision learners," in *CVPR*, pp. 16000–16009, 2022. **2, 4**
- [4] Z. Xie, Z. Zhang, Y. Cao, Y. Lin, J. Bao, Z. Yao, Q. Dai, and H. Hu, "Simmim: A simple framework for masked image modeling," in *CVPR*, pp. 9653–9663, 2022. **2, 4**
- [5] K. He, H. Fan, Y. Wu, S. Xie, and R. Girshick, "Momentum contrast for unsupervised visual representation learning," in *CVPR*, pp. 9729–9738, 2020. **2, 4**
- [6] N. Houlsby, A. Giurgiu, S. Jastrzebski, B. Morrone, Q. De Laroussilhe, A. Gesmundo, M. Attariyan, and S. Gelly, "Parameter-efficient transfer learning for nlp," in *ICLR*, pp. 2790–2799, PMLR, 2019. **3**
- [7] C. Deng, D. Jing, Y. Han, and J. Chanussot, "Towards hierarchical adaptive alignment for aerial object detection in remote sensing images," *IEEE TGRS*, 2023. **4**
- [8] J. Zhu, X. Chen, H. Zhang, Z. Tan, S. Wang, and H. Ma, "Transformer based remote sensing object detection with enhanced multispectral feature extraction," *IEEE Geoscience and Remote Sensing Letters*, vol. 20, pp. 1–5, 2023. **4**
- [9] S. Low, O. Nina, D. Bowald, A. D. Sappa, N. Inkawich, and P. Bruns, "Multi-modal aerial view image challenge: Sar classification," in *CVPR*, pp. 3105–3112, 2024. **4**
- [10] Y. Li, S. Li, H. Du, L. Chen, D. Zhang, and Y. Li, "Yolo-acn: Focusing on small target and occluded object detection," *IEEE Access*, vol. 8, pp. 227288–227303, 2020. **4**
- [11] X. Li, W. Diao, Y. Mao, P. Gao, X. Mao, X. Li, and X. Sun, "Ogmn: Occlusion-guided multi-task network for object detection in uav images," *ISPRS Journal of Photogrammetry and Remote Sensing*, vol. 199, pp. 242–257, 2023. **4, 11**
- [12] A. Wang, Y. Sun, A. Kortylewski, and A. L. Yuille, "Robust object detection under occlusion with context-aware compositionalnets," in *CVPR*, pp. 12645–12654, 2020. **4**
- [13] T. Ye, W. Qin, Z. Zhao, X. Gao, X. Deng, and Y. Ouyang, "Real-time object detection network in uav-vision based on cnn and transformer," *IEEE Transactions on Instrumentation and Measurement*, vol. 72, pp. 1–13, 2023. **4**
- [14] Y. Liu, F. Yang, and P. Hu, "Small-object detection in uav-captured images via multi-branch parallel feature pyramid networks," *IEEE Access*, vol. 8, pp. 145740–145750, 2020. **4**
- [15] L. Tan, X. Lv, X. Lian, and G. Wang, "Yolov4_drone: Uav image target detection based on an improved yolov4 algorithm," *Computers & Electrical Engineering*, vol. 93, p. 107261, 2021. **4**
- [16] Y. Huang, J. Chen, and D. Huang, "Ufpmp-det: Toward accurate and efficient object detection on drone imagery," in *AAAI*, vol. 36, pp. 1026–1033, 2022. **4**
- [17] C. Yang, Z. Huang, and N. Wang, "Querydet: Cascaded sparse query for accelerating high-resolution small object detection," in *CVPR*, pp. 13668–13677, 2022. **4, 11**
- [18] W. Weng, M. Wei, J. Ren, and F. Shen, "Enhancing aerial object detection with selective frequency interaction network," *IEEE Transactions on Artificial Intelligence*, 2024. **4**
- [19] J. Li, S. Zhang, Y. Sun, Q. Han, Y. Sun, and Y. Wang, "Frequency-driven edge guidance network for semantic segmentation of remote sensing images," *IEEE JSTARS*, 2024. **4**
- [20] K. Simonyan and A. Zisserman, "Very deep convolutional networks for large-scale image recognition," in *3rd International Conference on Learning Representations (ICLR 2015)*, Computational and Biological Learning Society, 2015. **4**
- [21] K. He, X. Zhang, S. Ren, and J. Sun, "Deep residual learning for image recognition," in *CVPR*, pp. 770–778, 2016. **4**
- [22] J. Deng, W. Dong, R. Socher, L.-J. Li, K. Li, and L. Fei-Fei, "Imagenet: A large-scale hierarchical image database," in *CVPR*, pp. 248–255, Ieee, 2009. **4, 13**
- [23] A. Dosovitskiy, L. Beyer, A. Kolesnikov, D. Weissenborn, X. Zhai, T. Unterthiner, M. Dehghani, M. Minderer, G. Heigold, S. Gelly, *et al.*, "An image is worth 16x16 words: Transformers for image recognition at scale," *arXiv preprint arXiv:2010.11929*, 2020. **4**
- [24] Z. Liu, Y. Lin, Y. Cao, H. Hu, Y. Wei, Z. Zhang, S. Lin, and B. Guo, "Swin transformer: Hierarchical vision transformer using shifted windows," in *ICCV*, pp. 10012–10022, 2021. **4**
- [25] Z. Liu, H. Mao, C.-Y. Wu, C. Feichtenhofer, T. Darrell, and S. Xie, "A convnet for the 2020s," in *CVPR*, pp. 11976–11986, 2022. **4**

[26] A. Gu and T. Dao, "Mamba: Linear-time sequence modeling with selective state spaces," *arXiv preprint arXiv:2312.00752*, 2023. 4

[27] X. Chen, H. Fan, R. Girshick, and K. He, "Improved baselines with momentum contrastive learning," *arXiv preprint arXiv:2003.04297*, 2020. 4

[28] X. Chen, S. Xie, and K. He, "An empirical study of training self-supervised vision transformers," in *ICCV*, pp. 9640–9649, 2021. 4

[29] T. Chen, S. Kornblith, M. Norouzi, and G. Hinton, "A simple framework for contrastive learning of visual representations," in *ICLR*, pp. 1597–1607, PMLR, 2020. 4

[30] X. Chen and K. He, "Exploring simple siamese representation learning," in *CVPR*, pp. 15750–15758, 2021. 4

[31] M. Caron, H. Touvron, I. Misra, H. Jégou, J. Mairal, P. Bojanowski, and A. Joulin, "Emerging properties in self-supervised vision transformers," in *ICCV*, pp. 9650–9660, 2021. 4

[32] H. Li, Y. Li, G. Zhang, R. Liu, H. Huang, Q. Zhu, and C. Tao, "Global and local contrastive self-supervised learning for semantic segmentation of hr remote sensing images," *IEEE TGRS*, vol. 60, pp. 1–14, 2022. 4

[33] O. Manas, A. Lacoste, X. Giró-i Nieto, D. Vazquez, and P. Rodriguez, "Seasonal contrast: Unsupervised pre-training from uncurated remote sensing data," in *ICCV*, pp. 9414–9423, 2021. 4, 12

[34] J. Liu, X. Huang, J. Zheng, Y. Liu, and H. Li, "Mixmim: Mixed and masked image modeling for efficient visual representation learning," 2022. 4

[35] L. Huang, S. You, M. Zheng, F. Wang, C. Qian, and T. Yamasaki, "Green hierarchical vision transformer for masked image modeling," *NeurIPS*, vol. 35, pp. 19997–20010, 2022. 4

[36] X. Li, W. Wang, L. Yang, and J. Yang, "Uniform masking: Enabling mae pre-training for pyramid-based vision transformers with locality," *arXiv preprint arXiv:2205.10063*, 2022. 4

[37] X. Chen, M. Ding, X. Wang, Y. Xin, S. Mo, Y. Wang, S. Han, P. Luo, G. Zeng, and J. Wang, "Context autoencoder for self-supervised representation learning," *IJCV*, vol. 132, no. 1, pp. 208–223, 2024. 4

[38] Z. Huang, X. Jin, C. Lu, Q. Hou, M.-M. Cheng, D. Fu, X. Shen, and J. Feng, "Contrastive masked autoencoders are stronger vision learners," *IEEE TPAMI*, 2023. 5

[39] Q. Zhou, C. Yu, H. Luo, Z. Wang, and H. Li, "Mimco: Masked image modeling pre-training with contrastive teacher," in *ACM Multimedia*, pp. 4487–4495, 2022. 5

[40] X. Cao, H. Lin, S. Guo, T. Xiong, and L. Jiao, "Transformer-based masked autoencoder with contrastive loss for hyperspectral image classification," *IEEE TGRS*, 2023. 5

[41] Z. Li, H. Chen, J. Wu, J. Li, and N. Jing, "Segmind: Semi-supervised remote sensing image semantic segmentation with masked image modeling and contrastive learning method," *IEEE TGRS*, 2023. 5

[42] L.-C. Chen, Y. Zhu, G. Papandreou, F. Schroff, and H. Adam, "Encoder-decoder with atrous separable convolution for semantic image segmentation," in *ECCV*, pp. 801–818, 2018. 9, 10

[43] J. Fu, J. Liu, H. Tian, Y. Li, Y. Bao, Z. Fang, and H. Lu, "Dual attention network for scene segmentation," in *CVPR*, pp. 3146–3154, 2019. 9, 10

[44] X. Ding, Y. Guo, G. Ding, and J. Han, "Acnet: Strengthening the kernel skeletons for powerful cnn via asymmetric convolution blocks," in *ICCV*, pp. 1911–1920, 2019. 9, 10

[45] Y. Yuan, X. Chen, and J. Wang, "Object-contextual representations for semantic segmentation," in *ECCV*, pp. 173–190, Springer, 2020. 9, 10

[46] S. Zheng, J. Lu, H. Zhao, X. Zhu, Z. Luo, Y. Wang, Y. Fu, J. Feng, T. Xiang, P. H. Torr, *et al.*, "Rethinking semantic segmentation from a sequence-to-sequence perspective with transformers," in *CVPR*, pp. 6881–6890, 2021. 9, 10

[47] E. Xie, W. Wang, Z. Yu, A. Anandkumar, J. M. Alvarez, and P. Luo, "Segformer: Simple and efficient design for semantic segmentation with transformers," *NeurIPS*, vol. 34, pp. 12077–12090, 2021. 9, 10

[48] X. Dong, J. Bao, D. Chen, W. Zhang, N. Yu, L. Yuan, D. Chen, and B. Guo, "Cswin transformer: A general vision transformer backbone with cross-shaped windows," in *CVPR*, pp. 12124–12134, 2022. 9, 10

[49] S. Yi, X. Liu, J. Li, and L. Chen, "Uavformer: A composite transformer network for urban scene segmentation of uav images," *Pattern Recognition*, vol. 133, p. 109019, 2023. 9, 10

[50] C. Yu, C. Gao, J. Wang, G. Yu, C. Shen, and N. Sang, "Bisenet v2: Bilateral network with guided aggregation for real-time semantic segmentation," *IJCV*, vol. 129, pp. 3051–3068, 2021. 9

[51] R. Strudel, R. Garcia, I. Laptev, and C. Schmid, "Segmenter: Transformer for semantic segmentation," in *ICCV*, pp. 7262–7272, 2021. 9

[52] W. Xu, Y. Xu, T. Chang, and Z. Tu, "Co-scale conv-attentional image transformers," in *ICCV*, pp. 9981–9990, 2021. 9

[53] Y. Chen, G. Lin, S. Li, O. Bourahla, Y. Wu, F. Wang, J. Feng, M. Xu, and X. Li, "Banet: Bidirectional aggregation network with occlusion handling for panoptic segmentation," in *CVPR*, pp. 3793–3802, 2020. 9

[54] L. Wang, R. Li, C. Zhang, S. Fang, C. Duan, X. Meng, and P. M. Atkinson, "Unetformer: A unet-like transformer for efficient semantic segmentation of remote sensing urban scene imagery," *ISPRS Journal of Photogrammetry and Remote Sensing*, vol. 190, pp. 196–214, 2022. 9

[55] S. Chen, C. Ge, Z. Tong, J. Wang, Y. Song, J. Wang, and P. Luo, "Adaptformer: Adapting vision transformers for scalable visual recognition," *NeurIPS*, vol. 35, pp. 16664–16678, 2022. 9

[56] V. Badrinarayanan, A. Kendall, and R. Cipolla, "Segnet: A deep convolutional encoder-decoder architecture for image segmentation," *IEEE TPAMI*, vol. 39, no. 12, pp. 2481–2495, 2017. 10

[57] J. Long, E. Shelhamer, and T. Darrell, "Fully convolutional networks for semantic segmentation," in *CVPR*, pp. 3431–3440, 2015. 10

[58] H. Zhao, J. Shi, X. Qi, X. Wang, and J. Jia, "Pyramid scene parsing network," in *CVPR*, pp. 2881–2890, 2017. 10

[59] L.-C. Chen, G. Papandreou, I. Kokkinos, K. Murphy, and A. L. Yuille, "Deeplab: Semantic image segmentation with deep convolutional nets, atrous convolution, and fully connected crfs," *IEEE TPAMI*, vol. 40, no. 4, pp. 834–848, 2017. 10

[60] O. Ronneberger, P. Fischer, and T. Brox, "U-net: Convolutional networks for biomedical image segmentation," in *MICCAI*, pp. 234–241, Springer, 2015. 10

[61] K. Sun, B. Xiao, D. Liu, and J. Wang, "Deep high-resolution representation learning for human pose estimation," in *CVPR*, pp. 5693–5703, 2019. 10

[62] J. Chen, Y. Lu, Q. Yu, X. Luo, E. Adeli, Y. Wang, L. Lu, A. L. Yuille, and Y. Zhou, "Transunet: Transformers make strong encoders for medical image segmentation," *arXiv preprint arXiv:2102.04306*, 2021. 10

[63] Z. Li, C. Peng, G. Yu, X. Zhang, Y. Deng, and J. Sun, "Light-head r-cnn: In defense of two-stage object detector," *arXiv preprint arXiv:1711.07264*, 2017. 11

[64] H. Law and J. Deng, "Cornernet: Detecting objects as paired keypoints," in *ECCV*, pp. 734–750, 2018. 11

[65] T.-Y. Lin, P. Goyal, R. Girshick, K. He, and P. Dollár, "Focal loss for dense object detection," in *ICCV*, pp. 2980–2988, 2017. 11, 12

[66] A. Bochkovskiy, C.-Y. Wang, and H.-Y. M. Liao, "Yolov4: Optimal speed and accuracy of object detection," *arXiv preprint arXiv:2004.10934*, 2020. 11

[67] Z. Cai and N. Vasconcelos, "Cascade r-cnn: High quality object detection and instance segmentation," *IEEE TPAMI*, vol. 43, no. 5, pp. 1483–1498, 2019. 11, 12, 15, 18

[68] Y. Lin, J. Zhang, and J. Huang, "Centralised visual processing center for remote sensing target detection," *Scientific Reports*, vol. 14, no. 1, p. 17021, 2024. 11

[69] J. Chen, R. Wen, and L. Ma, "Small object detection model for uav aerial image based on yolov7," *Signal, Image and Video Processing*, vol. 18, no. 3, pp. 2695–2707, 2024. 11

[70] L. Jiang, B. Yuan, J. Du, B. Chen, H. Xie, J. Tian, and Z. Yuan, "Mffsodnet: Multi-scale feature fusion small object detection network for uav aerial images," *IEEE Transactions on Instrumentation and Measurement*, 2024. 11

[71] S. Deng, S. Li, K. Xie, W. Song, X. Liao, A. Hao, and H. Qin, "A global-local self-adaptive network for drone-view object detection," *IEEE TIP*, vol. 30, pp. 1556–1569, 2020. 11

[72] J. Wan, B. Zhang, Y. Zhao, Y. Du, and Z. Tong, "Vistrongerdet: Stronger visual information for object detection in visdrone images," in *ICCV*, pp. 2820–2829, 2021. 11

[73] W. Li, X. Zhang, Y. Peng, and M. Dong, "Dmnet: A network architecture using dilated convolution and multiscale mechanisms for spatiotemporal fusion of remote sensing images," *IEEE Sensors Journal*, vol. 20, no. 20, pp. 12190–12202, 2020. 11

[74] Z. Liu, G. Gao, L. Sun, and Z. Fang, "Hrdnet: High-resolution detection network for small objects," in *ICME*, pp. 1–6, IEEE, 2021. [11](#)

[75] F. Yang, H. Fan, P. Chu, E. Blasch, and H. Ling, "Clustered object detection in aerial images," in *ICCV*, pp. 8311–8320, 2019. [11](#)

[76] N. Yin, C. Liu, R. Tian, and X. Qian, "Sdpdet: Learning scale-separated dynamic proposals for end-to-end drone-view detection," *IEEE Transactions on Multimedia*, 2024. [11](#)

[77] Z. Wei, C. Duan, X. Song, Y. Tian, and H. Wang, "Amrnet: Chips augmentation in aerial images object detection," *arXiv preprint arXiv:2009.07168*, 2020. [11](#)

[78] S. Zhang, X. Wang, J. Wang, J. Pang, C. Lyu, W. Zhang, P. Luo, and K. Chen, "Dense distinct query for end-to-end object detection," in *CVPR*, pp. 7329–7338, 2023. [11](#)

[79] Y. Fu, X. Zhang, and M. Wang, "Dshnet: A semantic segmentation model of remote sensing images based on dual stream hybrid network," *IEEE JSTARS*, 2024. [11](#)

[80] M. Tan, R. Pang, and Q. V. Le, "Efficientdet: Scalable and efficient object detection," in *CVPR*, pp. 10781–10790, 2020. [11](#)

[81] H. Shen, D. Lin, and T. Song, "Object detection deployed on uavs for oblique images by fusing imu information," *IEEE Geoscience and Remote Sensing Letters*, vol. 19, pp. 1–5, 2022. [11](#)

[82] X. Zhu, S. Lyu, X. Wang, and Q. Zhao, "Tph-yolov5: Improved yolov5 based on transformer prediction head for object detection on drone-captured scenarios," in *ICCV*, pp. 2778–2788, 2021. [11](#)

[83] C.-Y. Wang, A. Bochkovskiy, and H.-Y. M. Liao, "Yolov7: Trainable bag-of-freebies sets new state-of-the-art for real-time object detectors," in *CVPR*, pp. 7464–7475, 2023. [11](#)

[84] R. Lyu, "Nanodet-plus: Super fast and high accuracy lightweight anchor-free object detection model, 2021." [11](#)

[85] Z. Ge, S. Liu, F. Wang, Z. Li, and J. Sun, "Yolox: Exceeding yolo series in 2021," *arXiv preprint arXiv:2107.08430*, 2021. [11](#)

[86] K. Duan, S. Bai, L. Xie, H. Qi, Q. Huang, and Q. Tian, "Centernet++ for object detection," *IEEE TPAMI*, 2023. [11](#)

[87] G. Yu, Q. Chang, W. Lv, C. Xu, C. Cui, W. Ji, Q. Dang, K. Deng, G. Wang, Y. Du, et al., "Pp-picodet: A better real-time object detector on mobile devices," *arXiv preprint arXiv:2111.00902*, 2021. [11](#)

[88] S. Ren, "Faster r-cnn: Towards real-time object detection with region proposal networks," *arXiv preprint arXiv:1506.01497*, 2015. [11](#)

[89] J. Ding, N. Xue, Y. Long, G.-S. Xia, and Q. Lu, "Learning roi transformer for oriented object detection in aerial images," in *CVPR*, pp. 2849–2858, 2019. [11](#)

[90] J. Han, J. Ding, J. Li, and G.-S. Xia, "Align deep features for oriented object detection," *IEEE TGRS*, vol. 60, pp. 1–11, 2021. [11](#)

[91] X. Xie, G. Cheng, J. Wang, X. Yao, and J. Han, "Oriented r-cnn for object detection," in *ICCV*, pp. 3520–3529, 2021. [11](#)

[92] Y. Sun, B. Cao, P. Zhu, and Q. Hu, "Drone-based rgb-infrared cross-modality vehicle detection via uncertainty-aware learning," *IEEE Transactions on Circuits and Systems for Video Technology*, vol. 32, no. 10, pp. 6700–6713, 2022. [11](#)

[93] J. Wagner, V. Fischer, M. Herman, S. Behnke, et al., "Multispectral pedestrian detection using deep fusion convolutional neural networks," in *ESANN*, vol. 587, pp. 509–514, 2016. [11](#)

[94] L. Zhang, Z. Liu, S. Zhang, X. Yang, H. Qiao, K. Huang, and A. Hussain, "Cross-modality interactive attention network for multispectral pedestrian detection," *Information Fusion*, vol. 50, pp. 20–29, 2019. [11](#)

[95] C. Bao, J. Cao, Q. Hao, Y. Cheng, Y. Ning, and T. Zhao, "Dual-yolo architecture from infrared and visible images for object detection," *Sensors*, vol. 23, no. 6, p. 2934, 2023. [11](#)

[96] K. Ayush, B. Uzkent, C. Meng, K. Tanmay, M. Burke, D. Lobell, and S. Ermon, "Geography-aware self-supervised learning," in *ICCV*, pp. 10181–10190, 2021. [12](#)

[97] Y. Cong, S. Khanna, C. Meng, P. Liu, E. Rozi, Y. He, M. Burke, D. Lobell, and S. Ermon, "Satmae: Pre-training transformers for temporal and multi-spectral satellite imagery," *NeurIPS*, vol. 35, pp. 197–211, 2022. [12](#)

[98] D. Wang, Q. Zhang, Y. Xu, J. Zhang, B. Du, D. Tao, and L. Zhang, "Advancing plain vision transformer toward remote sensing foundation model," *IEEE TGRS*, vol. 61, pp. 1–15, 2022. [12](#)

[99] X. Wanyan, S. Seneviratne, S. Shen, and M. Kirley, "Dino-mc: Self-supervised contrastive learning for remote sensing imagery with multi-sized local crops," *arXiv preprint arXiv:2303.06670*, 2023. [12](#)

[100] C. Tao, J. Qi, G. Zhang, Q. Zhu, W. Lu, and H. Li, "Tov: The original vision model for optical remote sensing image understanding via self-supervised learning," *IEEE JSTARS*, vol. 16, pp. 4916–4930, 2023. [12](#)

[101] Y. Wang, N. A. A. Braham, Z. Xiong, C. Liu, C. M. Albrecht, and X. X. Zhu, "Ssl4eo-s12: A large-scale multimodal, multitemporal dataset for self-supervised learning in earth observation [software and data sets]," *IEEE Geoscience and Remote Sensing Magazine*, vol. 11, no. 3, pp. 98–106, 2023. [12](#)

[102] D. Muhtar, X. Zhang, P. Xiao, Z. Li, and F. Gu, "Cmid: A unified self-supervised learning framework for remote sensing image understanding," *IEEE TGRS*, vol. 61, pp. 1–17, 2023. [12](#)

[103] U. Mall, B. Hariharan, and K. Bala, "Change-aware sampling and contrastive learning for satellite images," in *CVPR*, pp. 5261–5270, 2023. [12](#)

[104] A. Fuller, K. Millard, and J. Green, "Croma: Remote sensing representations with contrastive radar-optical masked autoencoders," *NeurIPS*, vol. 36, 2024. [12](#)

[105] F. Bastani, P. Wolters, R. Gupta, J. Ferdinando, and A. Kembhavi, "Satlaspretrain: A large-scale dataset for remote sensing image understanding," in *ICCV*, pp. 16772–16782, 2023. [12](#)

[106] M. Mendieta, B. Han, X. Shi, Y. Zhu, and C. Chen, "Towards geospatial foundation models via continual pretraining," in *ICCV*, pp. 16806–16816, 2023. [12](#)

[107] C. J. Reed, R. Gupta, S. Li, S. Brockman, C. Funk, B. Clipp, K. Keutzer, S. Candido, M. Uyttendaele, and T. Darrell, "Scalemae: A scale-aware masked autoencoder for multiscale geospatial representation learning," in *ICCV*, pp. 4088–4099, 2023. [12](#)

[108] R. C. Daudt, B. Le Saux, and A. Boulch, "Fully convolutional siamese networks for change detection," in *ICIP*, pp. 4063–4067, IEEE, 2018. [12](#)

[109] C. Zhang, P. Yue, D. Tapete, L. Jiang, B. Shangguan, L. Huang, and G. Liu, "A deeply supervised image fusion network for change detection in high resolution bi-temporal remote sensing images," *ISPRS Journal of Photogrammetry and Remote Sensing*, vol. 166, pp. 183–200, 2020. [12](#)

[110] H. Chen and Z. Shi, "A spatial-temporal attention-based method and a new dataset for remote sensing image change detection," *Remote Sensing*, vol. 12, no. 10, p. 1662, 2020. [12](#)

[111] H. Chen, Z. Qi, and Z. Shi, "Remote sensing image change detection with transformers," *IEEE TGRS*, vol. 60, pp. 1–14, 2021. [12](#)

[112] S. Fang, K. Li, J. Shao, and Z. Li, "Snuenet-cd: A densely connected siamese network for change detection of vhr images," *IEEE Geoscience and Remote Sensing Letters*, vol. 19, pp. 1–5, 2021. [12](#)

[113] W. G. C. Bandara and V. M. Patel, "A transformer-based siamese network for change detection," *arXiv preprint arXiv:2201.01293*, 2022. [12](#)

[114] C. Barnes, E. Shechtman, A. Finkelstein, and D. B. Goldman, "PatchMatch: A randomized correspondence algorithm for structural image editing," *ACM Transactions on Graphics*, vol. 28, no. 3, p. 24, 2009. [13](#)

[115] Z. Yu and S. Gao, "Fast-mvsnet: Sparse-to-dense multi-view stereo with learned propagation and gauss-newton refinement," in *CVPR*, pp. 1949–1958, 2020. [13](#)

[116] Y. Yao, Z. Luo, S. Li, T. Fang, and L. Quan, "Mvsnet: Depth inference for unstructured multi-view stereo," in *ECCV*, pp. 767–783, 2018. [13](#)

[117] Y. Yao, Z. Luo, S. Li, T. Shen, T. Fang, and L. Quan, "Recurrent mvsnet for high-resolution multi-view stereo depth inference," in *CVPR*, pp. 5525–5534, 2019. [13](#)

[118] J. Liu and S. Ji, "A novel recurrent encoder-decoder structure for large-scale multi-view stereo reconstruction from an open aerial dataset," in *CVPR*, pp. 6050–6059, 2020. [13](#)

[119] X. Gu, Z. Fan, S. Zhu, Z. Dai, F. Tan, and P. Tan, "Cascade cost volume for high-resolution multi-view stereo and stereo matching," in *CVPR*, pp. 2495–2504, 2020. [13](#)

[120] B. Shuai, A. Berneshawi, X. Li, D. Modolo, and J. Tighe, "Siammot: Siamese multi-object tracking," in *CVPR*, pp. 12372–12382, 2021. [13](#)

[121] Y. Zhang, P. Sun, Y. Jiang, D. Yu, F. Weng, Z. Yuan, P. Luo, W. Liu, and X. Wang, "Bytetrack: Multi-object tracking by associating every detection box," in *ECCV*, pp. 1–21, Springer, 2022. [13](#)

[122] S. Liu, X. Li, H. Lu, and Y. He, "Multi-object tracking meets moving uav," in *CVPR*, pp. 8876–8885, 2022. [13](#)

[123] G. Maggiolino, A. Ahmad, J. Cao, and K. Kitani, "Deep oc-sort: Multi-pedestrian tracking by adaptive re-identification," in *ICIP*, pp. 3025–3029, IEEE, 2023. [13](#)

[124] F. Zeng, B. Dong, Y. Zhang, T. Wang, X. Zhang, and Y. Wei, "Motr: End-to-end multiple-object tracking with transformer," in *ECCV*, pp. 659–675, Springer, 2022. [13](#)

[125] T. Meinhhardt, A. Kirillov, L. Leal-Taixe, and C. Feichtenhofer, "Trackformer: Multi-object tracking with transformers," in *CVPR*, pp. 8844–8854, 2022. [13](#)

[126] M. Yao, J. Wang, J. Peng, M. Chi, and C. Liu, "Folt: Fast multiple object tracking from uav-captured videos based on optical flow," in *ACM Multimedia*, pp. 3375–3383, 2023. [13](#)

[127] K. Liu, S. Jin, Z. Fu, Z. Chen, R. Jiang, and J. Ye, "Uncertainty-aware unsupervised multi-object tracking," in *ICCV*, pp. 9996–10005, 2023. [13](#)

[128] J. Feng, D. Zeng, X. Jia, X. Zhang, J. Li, Y. Liang, and L. Jiao, "Cross-frame keypoint-based and spatial motion information-guided networks for moving vehicle detection and tracking in satellite videos," *ISPRS Journal of Photogrammetry and Remote Sensing*, vol. 177, pp. 116–130, 2021. [13](#)

[129] J. Cao, J. Pang, X. Weng, R. Khirodkar, and K. Kitani, "Observation-centric sort: Rethinking sort for robust multi-object tracking," in *CVPR*, pp. 9686–9696, 2023. [13](#)

[130] Y. Du, Z. Zhao, Y. Song, Y. Zhao, F. Su, T. Gong, and H. Meng, "Strongsort: Make deepsort great again," *IEEE Transactions on Multimedia*, vol. 25, pp. 8725–8737, 2023. [13](#)

[131] X. Zhou, V. Koltun, and P. Krähenbühl, "Tracking objects as points," in *ECCV*, pp. 474–490, Springer, 2020. [13](#)

[132] Q. He, X. Sun, Z. Yan, B. Li, and K. Fu, "Multi-object tracking in satellite videos with graph-based multitask modeling," *IEEE TGRS*, vol. 60, pp. 1–13, 2022. [13, 19](#)

[133] C. Xiao, S. Wu, Y. Wang, M. Li, W. An, and Z. Chen, "Rsmot: Remote sensing multi-object tracking network with local motion prior for objects in satellite videos," in *IGARSS*, pp. 1904–1907, IEEE, 2022. [13](#)

[134] L. Kong, Z. Yan, Y. Zhang, W. Diao, Z. Zhu, and L. Wang, "Cftracker: multi-object tracking with cross-frame connections in satellite videos," *IEEE TGRS*, vol. 61, pp. 1–14, 2023. [13](#)

[135] J. Wu, J. Cao, L. Song, Y. Wang, M. Yang, and J. Yuan, "Track to detect and segment: An online multi-object tracker," in *CVPR*, pp. 12352–12361, 2021. [13](#)

[136] C. Xiao, Q. Yin, X. Ying, R. Li, S. Wu, M. Li, L. Liu, W. An, and Z. Chen, "Dsfnet: Dynamic and static fusion network for moving object detection in satellite videos," *IEEE Geoscience and Remote Sensing Letters*, vol. 19, pp. 1–5, 2021. [13](#)

[137] Y. Zhang, C. Wang, X. Wang, W. Zeng, and W. Liu, "Fairmot: On the fairness of detection and re-identification in multiple object tracking," *IJCV*, vol. 129, pp. 3069–3087, 2021. [13](#)

[138] J. Peng, C. Wang, F. Wan, Y. Wu, Y. Wang, Y. Tai, C. Wang, J. Li, F. Huang, and Y. Fu, "Chained-tracker: Chaining paired attentive regression results for end-to-end joint multiple-object detection and tracking," in *ECCV*, pp. 145–161, Springer, 2020. [13](#)

[139] L. Ren, W. Yin, W. Diao, K. Fu, and X. Sun, "Motion-guided multi-object tracking model for high-speed aerial objects in satellite videos," *IEEE TGRS*, 2024. [13, 19](#)

[140] Y. Lyu, G. Vosselman, G.-S. Xia, A. Yilmaz, and M. Y. Yang, "Uavid: A semantic segmentation dataset for uav imagery," *ISPRS Journal of Photogrammetry and Remote Sensing*, vol. 165, pp. 108–119, 2020. [15](#)

[141] Y. Chen, Y. Wang, P. Lu, Y. Chen, and G. Wang, "Large-scale structure from motion with semantic constraints of aerial images," in *PRCV*, pp. 347–359, Springer, 2018. [15](#)

[142] M. Rahnmemoonfar, T. Chowdhury, A. Sarkar, D. Varshney, M. Yari, and R. R. Murphy, "Floodnet: A high resolution aerial imagery dataset for post flood scene understanding," *IEEE Access*, vol. 9, pp. 89644–89654, 2021. [15](#)

[143] M. Contributors, "MMSegmentation: Openmmlab semantic segmentation toolbox and benchmark." <https://github.com/open-mmlab/mmsegmentation>, 2020. [15](#)

[144] T. Xiao, Y. Liu, B. Zhou, Y. Jiang, and J. Sun, "Unified perceptual parsing for scene understanding," in *ECCV*, pp. 418–434, 2018. [15](#)

[145] B. Cheng, I. Misra, A. G. Schwing, A. Kirillov, and R. Girdhar, "Masked-attention mask transformer for universal image segmentation," in *CVPR*, pp. 1290–1299, 2022. [15](#)

[146] I. Loshchilov and F. Hutter, "Decoupled weight decay regularization," *arXiv preprint arXiv:1711.05101*, 2017. [15, 18](#)

[147] D. Du, P. Zhu, L. Wen, X. Bian, H. Lin, Q. Hu, T. Peng, J. Zheng, X. Wang, Y. Zhang, et al., "Visdrone-det2019: The vision meets drone object detection in image challenge results," in *ICCV Workshops*, pp. 0–0, 2019. [15](#)

[148] H. Yu, G. Li, W. Zhang, Q. Huang, D. Du, Q. Tian, and N. Sebe, "The unmanned aerial vehicle benchmark: Object detection, tracking and baseline," *IJCV*, vol. 128, pp. 1141–1159, 2020. [15](#)

[149] J. Zhao, Y. Chen, Z. Zhou, J. Zhao, S. Wang, and X. Chen, "Multiship speed measurement method based on machine vision and drone images," *IEEE Transactions on Instrumentation and Measurement*, vol. 72, pp. 1–12, 2023. [15](#)

[150] K. Chen, J. Wang, J. Pang, Y. Cao, Y. Xiong, X. Li, S. Sun, W. Feng, Z. Liu, J. Xu, Z. Zhang, D. Cheng, C. Zhu, T. Cheng, Q. Zhao, B. Li, X. Lu, R. Zhu, Y. Wu, J. Dai, J. Wang, J. Shi, W. Ouyang, C. C. Loy, and D. Lin, "MMDetection: Open mmlab detection toolbox and benchmark," *arXiv preprint arXiv:1906.07155*, 2019. [15, 19](#)

[151] M. Lebedev, Y. V. Vizilter, O. Vygolov, V. Knyaz, and A. Y. Rubis, "Change detection in remote sensing images using conditional adversarial networks," *International Archives of the Photogrammetry, Remote Sensing & Spatial Information Sciences*, vol. 42, no. 2, 2018. [16](#)

[152] G.-S. Xia, J. Hu, F. Hu, B. Shi, X. Bai, Y. Zhong, L. Zhang, and X. Lu, "Aid: A benchmark data set for performance evaluation of aerial scene classification," *IEEE TGRS*, vol. 55, no. 7, pp. 3965–3981, 2017. [18](#)

[153] G. Cheng, J. Han, and X. Lu, "Remote sensing image scene classification: Benchmark and state of the art," *Proceedings of the IEEE*, vol. 105, no. 10, pp. 1865–1883, 2017. [18](#)

[154] M. Contributors, "Openmmlab's pre-training toolbox and benchmark." <https://github.com/open-mmlab/mmpretrain>, 2023. [18](#)

[155] J. Li, X. Huang, Y. Feng, Z. Ji, S. Zhang, and D. Wen, "A hierarchical deformable deep neural network and an aerial image benchmark dataset for surface multiview stereo reconstruction," *IEEE TGRS*, vol. 61, pp. 1–12, 2023. [19](#)

[156] D. P. Kingma and J. Ba, "Adam: A method for stochastic optimization," *arXiv preprint arXiv:1412.6980*, 2014. [19](#)

[157] G. Chen, W. Wang, Z. He, L. Wang, Y. Yuan, D. Zhang, J. Zhang, P. Zhu, L. Van Gool, J. Han, et al., "Visdrone-mot2021: The vision meets drone multiple object tracking challenge results," in *ICCV*, pp. 2839–2846, 2021. [19](#)